

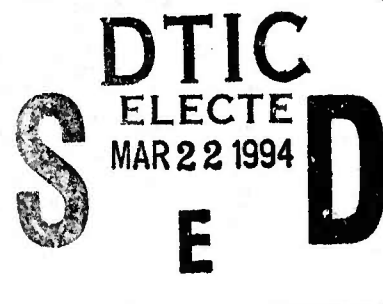
RL-TR-93-241  
Final Technical Report  
December 1993

AD-A277 287



# HIGH SPEED, STRAINED LAYER, MULTIQUANTUM WELL, GaInAsP AND GaAs LASERS AND HETEROSTRUCTURES

University of California at Santa Barbara



Sponsored by  
Advanced Research Projects Agency  
ARPA Order No. 7144

*APPROVED FOR PUBLIC RELEASE; DISTRIBUTION UNLIMITED.*

94-08995



The views and conclusions contained in this document are those of the authors and should not be interpreted as necessarily representing the official policies, either expressed or implied, of the Advanced Research Projects Agency or the U.S. Government.

Rome Laboratory  
Air Force Materiel Command  
Griffiss Air Force Base, New York

DTIC QUALITY INSPECTED 1

04 3 21 061

This report has been reviewed by the Rome Laboratory Public Affairs Office (PA) and is releasable to the National Technical Information Service (NTIS). At NTIS it will be releasable to the general public, including foreign nations.

RL-TR-93-241 has been reviewed and is approved for publication.

APPROVED:



JOSEPH P. LORENZO  
Project Engineer

FOR THE COMMANDER:



JOHN K. SCHINDLER  
Director of Electromagnetics & Reliability

If your address has changed or if you wish to be removed from the Rome Laboratory mailing list, or if the addressee is no longer employed by your organization, please notify RL ( EROC ) Hanscom AFB MA 01731. This will assist us in maintaining a current mailing list.

Do not return copies of this report unless contractual obligations or notices on a specific document require that it be returned.

HIGH SPEED, STRAINED LAYER, MULTIQUANTUM WELL,  
GaInAsP AND GaAs LASERS AND HETEROSTRUCTURES

J. Bowers, L. Coldren, etal, USCB  
G.Y. Robinson, M.J. Hafich, etal, Colorado State University

Contractor: University of California at Santa Barbara  
Contract Number: F19628-89-K-0042  
Effective Date of Contract: 22 September 1989  
Contract Expiration Date: 22 September 1992  
Short Title of Work: High Speed, Strained Layer,  
Mulltiquantum Well, GaInAsP and  
GaAs Lasers & Heterostructures

Program Code Number: 2E20  
Period of Work Covered: Sep 89 - Sep 92

Principal Investigator: Professors John Bowers, Larry  
Coldren, & Gary Robinson  
Phone: (805) 893-8447  
RL Project Engineer: Joseph Lorenzo  
Phone: (617) 377-2234

Approved for public release; distribution unlimited.

This research was supported by the Advanced Research  
Projects Agency of the Department of Defense and was  
monitored by Joseph Lorenzo, RL (EROC), 80 Scott Drive,  
Hanscom AFB MA 01731-5000 under Contract F19628-89-K-0042.

Accession For	
NTIS CRA&I	<input checked="checked" type="checkbox"/>
DTIC TAB	<input type="checkbox"/>
Unannounced	<input type="checkbox"/>
Justification _____	
By _____	
Distribution /	
Availability Codes	
Dist	Avail and/or Special
A-1	

# REPORT DOCUMENTATION PAGE

Form Approved  
OMB No. 0704-0188

Public reporting burden for this collection of information is estimated to average 1 hour per response, including the time for reviewing instructions, searching existing data sources, gathering and maintaining the data needed, and completing and reviewing the collection of information. Send comments regarding this burden estimate or any other aspect of this collection of information, including suggestions for reducing this burden, to Washington Headquarters Services, Directorate for Information Operations and Reports, 1215 Jefferson Davis Highway, Suite 1204, Arlington, VA 22202-4302, and to the Office of Management and Budget, Paperwork Reduction Project (0704-0188), Washington, DC 20503.

1. AGENCY USE ONLY (Leave Blank)		2. REPORT DATE December 1993		3. REPORT TYPE AND DATES COVERED Final -----	
4. TITLE AND SUBTITLE HIGH SPEED, STRAINED LAYER, MULTIQUANTUM WELL, GaInAsP AND GaAs LASERS AND HETEROSTRUCTURES				5. FUNDING NUMBERS C - F19628-89-K-0042 PE - 63201E PR - 7144 TA - AR WU - 01	
6. AUTHOR(S) J. Bowers, L. Coldren, et al, USCB G.Y. Robinson, M.J. Hafich, et al, Colorado State Univ.					
7. PERFORMING ORGANIZATION NAME(S) AND ADDRESS(ES) University of California at Santa Barbara Office of Research Development Santa Barbara CA 39106				8. PERFORMING ORGANIZATION REPORT NUMBER  N/A	
9. SPONSORING/MONITORING AGENCY NAME(S) AND ADDRESS(ES) Advanced Research Projects Agency 3701 North Fairfax Drive Arlington VA 22203-1714 Rome Laboratory (EROC) 80 Scott Drive Hanscom AFB MA 01631-5000				10. SPONSORING/MONITORING AGENCY REPORT NUMBER  RL-TR-93-241	
11. SUPPLEMENTARY NOTES Rome Laboratory Project Engineer: Joseph Lorenzo/EROC/(617) 377-2234					
12a. DISTRIBUTION/AVAILABILITY STATEMENT Approved for public release; distribution unlimited.				12b. DISTRIBUTION CODE	
13. ABSTRACT (Maximum 200 words) This report is divided into three Sections: the first covering the work done in the area of high speed InGaAs/GaAs strained quantum well lasers; the second in the material growth and laser fabrication in the InGaAs/AlInGaAs system; and the third in the Gas Source Molecular Beam Epitaxy (GSMBE) of In materials. This contract began at a time when quantum well laser bandwidths were severely limited for unknown reasons and the largest bandwidths were in bulk lasers. This has all changed now. Strained quantum well lasers were fabricated during the initial phase of this program resulting in anomalously large damping rates in quantum well lasers. Large damping rates result in small bandwidths because the lasers become critically damped at a low frequency. During the second portion of the contract, a theory describing the reasons for the resonance frequency, damping frequency, K factor, intensity noise, internal efficiency injection efficiency and wavelength chirping has been derived. Theoretical and experimental evidence in this program shows that carrier transport can lead to significant low frequency parasitic-like rolloff that reduces the modulation response by as much as a factor of six in quantum well lasers.					
14. SUBJECT TERMS Semiconductor laser, heterostructures, quantum wells, strained				15. NUMBER OF PAGES 68	
				16. PRICE CODE	
17. SECURITY CLASSIFICATION OF REPORT UNCLASSIFIED	18. SECURITY CLASSIFICATION OF THIS PAGE UNCLASSIFIED	19. SECURITY CLASSIFICATION OF ABSTRACT UNCLASSIFIED	20. LIMITATION OF ABSTRACT  UL		

## Table of Contents

1. Summary .....	1
2. InGaAs/GaAs Strained High Speed Quantum Well Lasers .....	3
2.1 Introduction .....	4
2.2 Device Fabrication and Characterization .....	5
2.3 Carrier Transport Across the Separate Confinement Heterostructure .....	6
2.4 Effect of Cavity Length and Ridge Width Variation .....	9
2.5 Carrier Escape from the Quantum Well .....	10
2.6 Effects of Carrier Transport on Injection Efficiency and Chirping .....	11
Journal Publications .....	15
Conference Presentations .....	16
3. MBE Growth of (Al,Ga,In)As Strained Quantum Well Lasers on InP .....	28
3.1 Introduction .....	29
3.2 Material Growth and Characterization .....	29
3.3 Broad Area Laser Results .....	30
3.4 Ridge Laser Results .....	31
Journal Publications .....	32
Conference Presentations .....	32
4. Gas-Source Molecular Beam Epitaxy (GSMBE) Growth of InGaAsP .....	40
4.1 Introduction .....	41
4.2 Epitaxial Growth .....	41
4.3 Results And Discussion .....	43
References .....	46
Journal Publications .....	47
Conference Presentations .....	47

## 1. Summary

This report is divided into three Sections; the first covering the work done in the area of high speed InGaAs/GaAs strained quantum well lasers, the second in the material growth and laser fabrication in the InGaAs/AlInGaAs system, and the third in the Gas Source Molecular Beam Epitaxy(GSMBE) of InP materials. Here we will present a brief summary of the work performed under the contract for the past three years.

This contract began at a time when quantum well laser bandwidths were severely limited for unknown reasons and the largest bandwidths were in bulk lasers. There had been numerous predictions of increased bandwidth in quantum well lasers, but these predictions seemed to be incorrect. This has now all changed. During the initial portion of this contract, we fabricated strained quantum well lasers and discovered anomalously large damping rates in quantum well lasers. Large damping rates result in small bandwidths because the lasers become critically damped at a low frequency. During the second portion of the contract, we developed a theory describing the reasons for the small bandwidths in quantum well lasers that had been observed throughout the world. The effect of transport on resonance frequency, damping frequency,  $K$  factor, intensity noise, internal efficiency, injection efficiency and wavelength chirping has been derived. We have shown theoretically and experimentally that carrier transport can lead to significant low frequency parasitic-like rolloff that reduces the modulation response by as much as a factor of six in quantum well lasers. We have also shown that, in addition, it leads to a reduction in the effective differential gain and thus the resonance frequency, while the nonlinear gain compression factor remains largely unaffected by it. In the presence of significant transport effects, we have shown that the real limit to the maximum possible modulation bandwidth is much lower than the one predicted by the  $K$  factor alone. We also clearly demonstrate that as in the case of device optimization for high speed operation, one has to minimize the transport time across the optical and current confinement regions and maximize the escape time out of the quantum well active region, to maximize the internal and the injection efficiencies and minimize the wavelength chirping. Finally, we developed a process for high speed ridge waveguide laser fabrication and demonstrated bandwidths of 22 GHz in strained quantum well lasers. These transport results have been used by groups around the world, and bandwidths of up to 30 GHz have now been demonstrated.

One of the conclusions of the transport theory of modulation is the importance of rapid uniform filling of quantum wells. This is particularly a problem in long wavelength InGaAsP/InP lasers where the valence band discontinuity is quite large. The InGaAs/AlGaInAs system has much smaller valence band discontinuities and better electron confinement. The initial focus of our research was on materials growth and broad area laser fabrication. The superiority of digital alloys was demonstrated in lasers with record low losses ( $3 \text{ cm}^{-1}$ ) and low threshold current densities ( $290 \text{ A/cm}^2$ ). A ridge waveguide technology was developed for AlGaInAs/InP and low threshold (20 mA) CW lasers were demonstrated. Initial high speed measurements are encouraging with  $2 \text{ GHz/mW}^{-5}$  relaxation oscillation slope efficiencies demonstrated.

An interesting alternative to MOCVD growth of InGaAsP is GSMBE growth. This research at CSU focussed on the development of growth techniques for high quality InGaAsP heterostructures. InGaAsP films with compositions corresponding to bandgap emission at wavelengths from 1.1 to  $1.6 \mu\text{m}$  were grown over a range of V/III ratios. A lattice mismatch of less than  $5 \times 10^{-4}$  was reproducibly obtained. Much of this research focussed on the growth of epitaxial mirrors for vertical cavity lasers. Uniform thickness layers were demonstrated with thicknesses of 171 nm uniform to 5 nm over a  $6 \mu\text{m}$  growth. High resolution TEM pictures indicate an abruptness of 1-2 monolayers at the InP/InGaAsP interface and 2-3 monolayers at the InGaAsP/InP interface. Record reflectivities of 97% in InGaAsP/InP were demonstrated.

A second major use of GSMBE grown films was in the demonstration of high speed InGaAs photodetectors. A series of films were grown to demonstrate the importance of graded layers in low resistance contacts resulting in lower contact resistance. The result was a series of photodetectors with successively higher bandwidths, first 70 GHz and then 110 GHz, which is a record for the InP system.

## **SECTION 2**

### **InGaAs/GaAs Strained High Speed Quantum Well Lasers**



## 2.1 Introduction

The high speed dynamics in semiconductor lasers have been conventionally modeled using a set of two coupled first order linear differential equations; one for the carrier density and the other for the photon density in the cavity. From the small signal analysis of these rate equations, the resonance frequency and the damping rate of the resultant second order system can be written as;  $f_r = (1/2\pi) \sqrt{v_g g' S / \tau_p}$  and  $\gamma = g' S + \epsilon S / \tau_p$ , where  $v_g$  is the group velocity in the cavity,  $g'$  is the differential gain,  $S$  is the photon density,  $\tau_p$  is the photon lifetime and  $\epsilon$  is the gain compression factor. In this analysis, the intrinsic limit to the speed of operation of the laser is the cavity loss rate determined by the photon lifetime, the differential gain and the photon density.

The optical gain,  $g'$ , is photon density dependent, i.e. it saturates at high photon density levels, and this provides an additional source of damping. This nonlinear photon density dependence of optical gain is introduced into the rate equation formalism via a phenomenological gain compression factor,  $\epsilon$ . The gain or the differential gain in the laser cavity is then written as,  $g' = g_0 / (1 + \epsilon S)$ , and in the case of small  $\epsilon S$ , keeping only the linear term of the Taylor expansion, it is also sometimes written as  $g' = g_0 (1 - \epsilon S)$  where  $g_0$  is the differential gain component determined solely by material parameters and may also be carrier density dependent as in the case of quantum well active regions. The physical origins of the gain compression factor are primarily spectral hole burning and transient carrier heating. The damping rate,  $\gamma$ , varies linearly with  $f_r^2$ , and the proportionality constant is called the  $K$  factor;  $K = 4\pi^2 (\tau_p + \epsilon / v_g g_0)$ . The maximum possible intrinsic modulation bandwidth is determined solely by this factor,  $f_{\max} = \sqrt{2} \frac{2\pi}{K}$ , and thus  $K$  is often taken as a figure of merit for high speed semiconductor lasers. In practice, the maximum possible modulation bandwidth is usually limited by  $RC$  parasitics, device heating and maximum power handling capability of the laser, especially the facets.

Although this analysis is mostly adequate for the design of high speed semiconductor lasers with bulk active areas, it falls short in explaining the modulation properties of semiconductor laser structures with additional carrier and optical confinement regions, like the quantum well lasers. Lasers with quantum well active areas have been theoretically and experimentally shown to have enhanced differential gain over the bulk lasers. Additional enhancements can be obtained with the inclusion of strain,  $p$ -doping or modulation doping. This enhancement in *material* differential gain (as opposed to the *effective* differential gain which is affected by the carrier transport factors) led to theoretical predictions of increased modulation

bandwidth in quantum well lasers, where it is only recently that the modulation bandwidths have been comparable to or better the best bulk lasers. Initially, the smaller modulation bandwidths in quantum well lasers over the bulk ones were explained by either an increase in the nonlinear gain compression factor,  $\epsilon$ . It has been theoretically proposed that  $\epsilon$  is enhanced by quantum confinement, and the inclusion of strain increases it even more. Using the spectral holeburning model for the computation of the intrinsic  $\epsilon$  and its variation with quantum confinement, quantum well structures can be optimized for high speed operation. A well-barrier holeburning model was also proposed which concluded that there is an additional contribution to the intrinsic  $\epsilon$  which is structure dependent.

We have, through the work sponsored by this contract, shown that the carrier transport effects like diffusion across the separate confinement heterostructure, tunneling between the quantum wells and escape via thermionic emission out of the quantum well are also important and often the dominant limit in the quantum well lasers. In this Section we will cover the *major highlights* of the strained InGaAs/GaAs high speed semiconductor laser effort at UCSB for the duration of the contract. The details of the device design, analysis and fabrication are presented in the publications sponsored by the contract which have been listed at the end of the Section.

## 2.2 Device Fabrication and Characterization

All the epitaxial material used in the study were grown by molecular beam epitaxy (MBE) at UCSB. Broad area lasers are fabricated to evaluate the quality of the laser material. The broad area threshold current density is a good indication of the material quality and the epitaxial layer design. In addition, the data for internal quantum efficiency and internal loss can also be extracted from broad area measurements. The compiled broad area data for the wafers presented in this final study is given in Table 1. The best wafers have a threshold current density of 93 A/cm<sup>2</sup> and an internal of 4.3 cm<sup>-1</sup>.

Fig. 1 shows the polyimide buried ridge waveguide high speed laser structure used by us to minimize the device parasitic capacitance. A self aligned technique is used to fabricate the narrow ridge waveguide lasers. In the first step, narrow metal stripes of Pd/Zn/Pd/Au/Ni are lifted off to define the ridge width and form the contact to the p<sup>+</sup> GaAs cap layer. Pd/Zn/Pd/Au contacts have been reported to give very low contact resistances on p doped GaAs. A contact resistance of  $1 \times 10^{-6} \Omega\text{-cm}^2$  was measured for this structure using the transmission line method. The final Ni layer is deposited to act as a mask for the subsequent reactive ion etch (RIE) step. The ridges are dry etched using Cl<sub>2</sub> and the etch depth is precisely monitored *in-situ* using a He-

Ne laser. Using this method, narrow ridges of a desired height are fabricated in a very controlled and reproducible manner. The ridges are etched to a depth of 8500 Å. The p-contacts are annealed after this at 410 °C for 5 s. Polyimide (Ciba-Geigy Probimide 284) is then spun on and cured for one hour at 320 °C in a N<sub>2</sub> atmosphere. The cured polyimide is then dry etched by O<sub>2</sub>, which is stopped once the metal stripe is exposed. Au is then patterned over the exposed metal stripe, using lift off, to form the top contact to the laser. The wafer is then subsequently lapped and Ni/AuGe/Ni/Au combination is deposited as the contact to the n GaAs substrate. The n contact is annealed at 380 °C for 15 s.

Fig. 2 shows the variation of threshold current with stripe width for 170 µm cavity length MQW lasers with three quantum wells. The variation of threshold current with stripe width is only 0.66 mA/µm, and the linear extrapolated intercept is 3.87 mA. This intercept gives a measure of the leakage current and the lateral diffusion of carriers. These results show that it is possible to fabricate low threshold lasers with narrow ridge waveguides down to 1 µm with this process. The threshold current reaches a minimum at around the ridge width of 2 µm. The increase in threshold current at smaller ridge widths is due to the loss of lateral optical confinement factor in the narrower ridge waveguide structures. At these dimensions the optical mode is no longer completely confined to the ridge waveguide, and the index discontinuity at the semiconductor/polyimide interface begins to introduce a significant amount of optical loss.

Fig. 3 shows the threshold current variation with temperature for two SQW laser samples. Sample C has a 3000 Å wide SCH and Sample F has a 900 Å wide SCH. Both of them have large characteristic temperature,  $T_0$ , and the threshold current is very stable against variations in temperature. On closer examination of Fig. 3, one may notice that the  $T_0$  value is not constant throughout the measurement range, but instead increases at about room temperature. The values of  $T_0$  measured here for the InGaAs/GaAs lasers are large compared to those between 50 K and 70 K reported for InGaAsP lasers at room temperature. This suggests a good possibility of high speed operation of these lasers at elevated temperatures.

### 2.3 Carrier Transport Across the Separate Confinement Heterostructure

Lasers were fabricated from three SQW samples with different SCH widths; Sample A with 760 Å wide SCH, Sample B with 1500 Å wide SCH and Sample C with 3000 Å wide SCH, to investigate the effects of varying the transport time on the modulation response. Figs. 4 (a) and 4 (b) show the experimental C.W. modulation response of Samples A and C. The samples both have 300 µm long cavities and 2.5 µm wide ridges. Although the devices are identical

except for the SCH width, the modulation response of Sample C with the widest SCH region is completely damped at about half the output power level of Sample A, and the bandwidth of Sample A is six times that of Sample C at higher power levels. The maximum C.W. modulation bandwidth for Sample A is 18.1 GHz, which is the largest reported to date in SQW lasers.

The damped response of Sample C shows all the effects predicted by the transport model. The response is *similar* to one of a device which is limited by a low frequency parasitic-like rolloff. In this case it cannot be attributed to device parasitics because both devices had been identically processed. To ascertain this, the parasitics, including the bond wire inductance, were extracted from the  $S_{11}$  parameter measured at the input port to the laser mount, and in addition the series resistance was measured using the HP 4145B semiconductor parameter analyzer. The series resistance of the devices is 4  $\Omega$ . The rolloff frequency due to the device parasitics is about 25 GHz. From the fit to the low frequency rolloff in the modulation response of Sample C, the value of the transport time is determined to be about 54 ps for the 3000 Å SCH width.

Fig. 5 shows the variation of the -3 dB modulation bandwidth with the square root of optical power for Samples B and C. There is good agreement between the experiment and model over a large range of optical power, and the model accurately predicts the discontinuity, caused by carrier transport, in the -3 dB bandwidth for Sample C. The value for  $\epsilon$  is taken to be  $1.5 \times 10^{-17} \text{ cm}^{-3}$  throughout.

Fig. 6 shows the experimental variation in the -3 dB modulation bandwidth with SCH width at different power levels. These data are from Samples A, B and C. The optimum SCH width also corresponds roughly to the point at which the optical confinement factor is a maximum. For a narrow SCH, the bandwidth drops off due to decreasing confinement factor resulting in a larger threshold gain and thus a lower differential gain. At larger SCH widths, the combination of a decreasing confinement factor and increasing carrier transport time across the undoped regions of the SCH, limits the modulation bandwidth. At sufficiently high powers for wide SCH devices, the characteristic *drop* due to carrier transport appears in the modulation bandwidth curve.

The variation of differential gain and gain compression factor,  $\epsilon$ , with SCH width (Samples A, B and C) was obtained from the modulation response as well as the relative intensity noise spectra of these lasers. As shown in Fig. 7, the results from the modulation response agree with the data extracted from the noise spectra measurements. Fig. 7 shows that the gain compression factor slightly increases for larger SCH widths, but given the scatter in the

data, this variation of  $\epsilon$  with SCH is not significant, and this variation alone cannot explain the severe low frequency rolloff in Sample C with the widest SCH region.

The variation of the differential gain extracted from the modulation response and noise spectra measurements, which can be thought of as an *effective* differential gain, is in contrast to the results from the threshold gain measurements which predict an increasing differential gain value with increasing width of the SCH layer. Sample C with the lowest threshold current density has the lowest effective differential gain. This is again due to carrier transport which reduces the differential gain from  $g_0$  to  $g_0/\chi$ . This reduction in the differential gain is also responsible for the reduction in the resonance frequency at high power levels in Sample C compared to Sample A (Fig. 4 (a) compared to 4 (b)).

The additional low frequency rolloff present in the modulation response is absent in the relative intensity noise. For large values of carrier transport time the modulation bandwidth could be severely reduced, although the  $K$  factor values, which are affected by  $\chi$  alone and not the low frequency rolloff, as determined from the noise measurements could still be optimistic. It is generally believed that the noise spectrum measurement is a *parasitic free* means of determining the actual or potential modulation performance of a laser. In the presence of significant transport effects this is no longer true. Conventionally, the maximum possible modulation bandwidth in a semiconductor laser is determined by the  $K$  factor. In principle, if one could drive the laser to arbitrarily high output power levels without the deteriorating effects of device heating, then the maximum possible -3 dB bandwidth, in the absence of device parasitics, is given by this  $K$  factor limit. In the presence of carrier transport effects, the  $K$  factor is not only reduced due to the reduction in the effective differential gain, but also *no longer determines the maximum modulation bandwidth*, even in an otherwise perfect device.

Fig. 8 shows the modulation response and noise spectrum calculated using at a power level of 40 mW for a SQW laser with a SCH width of 3000 Å. The peak of the noise spectrum, which is a good indication of the resonance frequency in the presence of small damping, occurs at 10.9 GHz implying a maximum possible modulation bandwidth of 16.3 GHz at that power level. This is clearly a wrong conclusion as the *actual* bandwidth limited by carrier transport in this case is only 4.5 GHz.

Fig. 9 shows the maximum possible modulation bandwidth as a function of SCH width for a 300  $\mu\text{m}$  cavity length SQW laser. The dashed line shows the  $K$  factor limit which is commonly inferred from noise spectra measurements. The bold line is the *real limit* determined

by carrier transport across the SCH; this is the maximum that is possible before the low frequency rolloff due to transport becomes severe enough to cause a *sudden drop* in the variation of modulation bandwidth with increasing optical power. Herein lies the real danger of relying on  $K$  factors and  $RIN$  measurements to predict modulation bandwidths. A small  $K$  factor is indeed an indication of the good device and material quality, but one has to be careful as to the maximum modulation bandwidth limits implied by this quantity. One can truly use this as the limit only in devices where the carrier transport effects are minimal.

## 2.4 Effect of Cavity Length and Ridge Width Variation

One of the parameters that is significant, but not deliberately considered in the design process is the gain compression factor,  $\epsilon$ . Despite theoretical predictions that  $\epsilon$  is enhanced in quantum well lasers, and further enhanced by the presence of strain, our experimental evidence suggests to the contrary. The experimental data presented in Fig. 7 shows that the gain compression factor does not vary significantly with the SCH width. Our carrier transport model does not influence  $\epsilon$  at all. Fig. 10 shows the experimental variation of the gain compression factor with cavity length for SQW and MQW lasers. The gain compression factor is lower for shorter cavity lasers and lasers with smaller number of wells. In this case the lowest value of  $\epsilon$  is for a SQW laser of 200  $\mu\text{m}$  cavity length. This value of  $9.98 \times 10^{-18} \text{ cm}^{-3}$  is about 5 to 6 times lower than the values reported for MQW lasers operating at around 1.55  $\mu\text{m}$  wavelength. The higher values of gain compression for MQW lasers and lasers with longer cavity lengths indicate that this nonlinearity is enhanced by increasing quantum confinement of the carriers.

Fig. 11 shows the experimental and theoretical variation of modulation bandwidth with cavity length for SQW and MQW lasers. This data has been extracted from Samples F and G. The parasitics were more significant in this set of devices, and the  $RC$  product was about 14.5 ps. The effects of the parasitics have been deconvolved from the experimental data presented in Fig. 11. The SQW lasers exhibit a broad maximum for the cavity length dependence of modulation bandwidth while MQW lasers are generally more sensitive to cavity length variations. As the cavity length is reduced, the threshold gain increases leading to a decrease in the differential gain. This is balanced by the reduction in the photon lifetime, and this results in an optimum cavity length for the maximum modulation bandwidth.

Fig. 12 shows the variation of resonance frequency with square root of power for two 150  $\mu\text{m}$  long 3 QW devices (Sample D) that differ only in the width of the ridge waveguide. One of the drawbacks of a ridge waveguide structure for high speed applications is the lateral

carrier diffusion along the active area. This carrier diffusion is severe for wider ridges, and is known to introduce additional damping to the modulation response. From Fig. 12, the device with a  $2.5\text{ }\mu\text{m}$  wide ridge has a better response than one with a  $1.5\text{ }\mu\text{m}$  wide ridge. Lateral carrier diffusion is not the only concern when designing narrow ridge waveguide lasers. The loss of lateral confinement of the optical mode becomes severe for narrow ridges. This leads to an increase in the threshold current as the ridge width is reduced below about  $2\text{ }\mu\text{m}$  (see Fig. 2). Another area of concern is the poor thermal dissipation in narrow ridge waveguide lasers. These constraints lead to optimum ridge width of about  $2.5\text{ }\mu\text{m}$  for the best modulation performance.

## 2.5 Carrier Escape from the Quantum Well

The experimental data for the dependence of the high speed parameters on the thermionic emission time is obtained from two samples with different energy barriers in the SCH; Sample D with  $\text{Al}_{0.15}\text{Ga}_{0.85}\text{As}$  SCH and Sample E with GaAs SCH. Fig. 13 shows the variation of the resonance frequency with the square root of power obtained from the modulation response data for the two cases considered here. The resonance frequency for the MQW laser with  $\text{Al}_{0.15}\text{Ga}_{0.85}\text{As}$  SCH (higher barrier and hence a longer thermionic emission time) is almost twice that of the laser with GaAs SCH at equivalent power levels. The differential gain for Sample D is more than 2.5 times that of Sample E. The gain compression coefficient,  $\epsilon$ , for both cases is about the same. Both devices have a  $205\text{ }\mu\text{m}$  long cavity and a  $2\text{ }\mu\text{m}$  wide ridge.

The larger differential gain in the case of Sample D, with  $\text{Al}_{0.15}\text{Ga}_{0.85}\text{As}$  SCH, is surprising considering that it had a larger threshold gain, due to a larger internal loss and a smaller optical confinement factor. Consequently, due to gain saturation in quantum well lasers it is *expected* to have a lower differential gain. This result is consistent with the carrier transport model which attributes part of this discrepancy to the reduction in the *effective* or *dynamic* differential gain in Sample E due to an increase in  $\chi$  caused by a reduction in  $\tau_e$ . Further, the lower energy barrier and the larger density of states in SCH of Sample E, leads to a severe *carrier overflow* thereby causing a much slower rise in the quasi-Fermi levels under carrier injection. This reduces the differential gain even under *static* operating conditions.

Fig. 14 shows the modulation response of the laser sample optimized using the model developed here. This device which has a  $150\text{ }\mu\text{m}$  long cavity and a  $2.5\text{ }\mu\text{m}$  wide ridge, is from Sample D which has 3 QWs and an  $\text{Al}_{0.15}\text{Ga}_{0.85}\text{As}$  SCH. The maximum - 3 dB modulation bandwidth is about 22 GHz. The device is presently thermally limited. The performance can be



improved by having a lower internal loss in the material (see Table 1) which would lead to better external quantum efficiencies, and larger output powers at lower operating current levels.

## 2.6 Effects of Carrier Transport on Injection Efficiency and Chirping

Although initially the effects of carrier transport processes were exclusively studied in relation to the modulation dynamics in quantum well lasers, in a more recent publication we have established that these transport times also profoundly affect the static properties, like the internal and injection efficiency, of quantum well lasers. Generally, there is some confusion as to the usage of the term internal quantum efficiency with respect to light emitting devices. In this paper, we define the quantum efficiency or the internal efficiency,  $\eta_{int}$ , of a light emitting device to be the fraction of the total injected current that radiatively recombines to produce light output. This is the overall efficiency of the device. The injection efficiency,  $\eta_{inj}$ , on the other hand refers to the total fraction of the injected current that flows into the active region above threshold. There is no distinction made in the latter definition between the radiative and non-radiative current components in the active region.

Using our carrier transport model, the analytic expressions for the injection efficiency and the internal efficiency are derived as,

$$\eta_{int} = \frac{1}{1 + \frac{\tau_r}{\tau_e} \left( \frac{\tau_n}{\tau_b} \right) + \frac{\tau_r}{\tau_b} \left( 1 + \frac{\tau_n}{\tau_{nr}} \right) + \frac{\tau_n}{\tau_{nr}}}$$

$$\eta_{inj} = \frac{1 - \left( \left( 1 - \beta + \frac{\tau_n}{\tau_{nr}} \right) \left( 1 + \frac{\tau_r}{\tau_b} \right) + \frac{\tau_r}{\tau_e} \left( \frac{\tau_n}{\tau_b} \right) \right) \eta_{clamp}}{\left( 1 + \frac{\tau_r}{\tau_b} \right)}$$

In the equation above  $\tau_r$  is the transport time across the SCH,  $\tau_e$  is the effective thermionic emission time out of the quantum well,  $\beta$  is the spontaneous emission feedback factor,  $\epsilon$  is the gain compression factor,  $\tau_b$  is the total recombination lifetime in the confinement and barrier regions,  $\tau_n$  is the bimolecular recombination lifetime,  $\tau_{nr}$  is the non-radiative recombination lifetime in the quantum well active area, and  $N_w$  is the carrier number in the quantum well active area. Here, we have introduced a term called the 'clamping' efficiency,  $\eta_{clamp} =$



$d(N_{wo}/\tau_n)/d(I_o/q)$  which is the measure of how much the carrier density in the active area varies with injected current above threshold.

Fig. 15 shows the variation of both the internal and injection efficiencies with the width of the SCH structure. For this calculation we have taken  $\eta_{clamp}$  to have a constant value of 8%. This value for  $\eta_{clamp}$  gives an upper limit of little over 90% for  $\eta_{inj}$  which is about the maximum we have experimentally observed in our MQW and SQW devices.

From Fig. 16 it can also be seen that the internal efficiency is a strong function of the carrier confinement energy while the injection efficiency is only a little degraded for the lowest carrier confinement energies, i.e. for GaAs in the SCH. This apparent insensitivity of the injection efficiency is due to the constant value of 8% assumed for  $\eta_{clamp}$ . The  $\eta_{clamp}$  term should in principle also be a function of the confinement energy. We have not included this in our calculations.

The  $\eta_{clamp}$  term usually has some finite value mainly because of carrier heating, which causes a decrease in the gain with an increase in the injected current. This leads to a corresponding increase in the carrier density to maintain the original level of gain which is required to overcome the fixed losses in the laser. Another reason for the increase in carrier density in the active area with injected current above threshold is the variation in the lateral mode profile either from a transition to higher order lateral modes which have larger gain thresholds or an expansion of the width of lasing region above threshold due to current spreading. Since most of the  $\eta_{inj}$  measurements are made on broad area lasers or in lasers with wide ridge (50  $\mu\text{m}$  as in our case) waveguide structures, the lateral mode variation under current injection may be the more significant factor. This will be aggravated in the case of lasers with severe carrier transport problems, because the enhanced carrier density variation in the SCH region leads to an increase in the lateral current spreading component.

Carrier transport, especially carrier density variation in the SCH region, also has a significant impact on the wavelength chirping of high speed quantum well lasers under current modulation. In lasers with bulk active areas or in lasers with large optical confinement factors one needs to compute only the index variation due to changes in carrier density in the active area to determine the wavelength chirp. In quantum well lasers, which generally have fairly small optical confinement factors, carrier density variations and hence the index changes in the confinement regions become important.

In this analysis of wavelength chirping, the  $\alpha$  parameter is written in terms of an effective mode index as,

$$\alpha_{modal} = \frac{\partial n'_{eff} / \partial N}{\partial n''_{eff} / \partial N}$$

where the real and the imaginary components of the effective index of refraction are given by  $n'_{eff}$  and  $n''_{eff}$ . The definition in terms of the effective index quantities is consistent because both  $n'_{eff}$  and  $n''_{eff}$  are evaluated with respect to the same mode overlap integrals. The gain,  $g$ , and the imaginary part of the index of refraction are related;  $g = \frac{4\pi}{\lambda} n''$ , where  $\lambda$  is the emission wavelength of the laser. In terms of the effective index, this is written as,  $\Gamma g = \frac{4\pi}{\lambda} n''_{eff}$ , where  $\Gamma$  is the optical confinement factor. Thus, the change in the effective gain and the real part of the index of refraction (from here onwards called just the index) are related via an effective  $\alpha$  which is true only for the particular optical mode. Since the optical mode is generally different for different laser structures, this  $\alpha$  parameter is structure dependent. We have called this the modal  $\alpha$ . Although the  $\alpha$  as originally derived is purely a material parameter, the  $\alpha_{modal}$  defined here is affected by the structure dependent carrier transport parameters.

Using the carrier transport model, the final expression for  $\alpha_{modal}$  is,

$$\alpha_{modal} = \frac{4\pi}{\lambda g_o} \left( \frac{\partial n}{\partial N_{wo}} + \left( \frac{1}{\Gamma} - 1 \right) (\chi - 1) \eta_{inj,max} \frac{\partial n}{\partial N_{bo}} \right)$$

where  $g_o$  is the differential gain,  $N_{wo}$  is the steady state carrier density in the quantum well, and  $N_{bo}$  the steady state carrier density in the SCH region..

Fig. 17 shows the variation of  $\alpha_{modal}$  with the width of the SCH. For a given carrier confinement energy in the SCH, laser structures with wide SCH regions have a larger amount of wavelength chirping. This translates into a higher FM efficiencies in lasers with wider SCH region. This trend has also been experimentally observe. Wavelength chirping is also a sensitive function of the optical confinement factor. The MQW lasers with larger optical confinement factors have lower amounts of wavelength chirping under current modulation. The increase in the amount of chirp with the SCH width is due primarily to the increase in the carrier transport time which is proportional to the square of the SCH width, and the decrease in the optical confinement factor.

Laser structures with lower carrier confinement energies in the SCH layers also have larger  $\alpha_{\text{modal}}$ , and hence, larger amounts of wavelength chirping under current modulation. As shown in Fig. 18,  $\text{In}_{0.2}\text{Ga}_{0.8}\text{As}/\text{GaAs}$  lasers require Al mole fractions of at least 15% for the wavelength chirping to reach its minimum value. Here again MQW lasers have a lower amount of wavelength chirping compared to SQW lasers. The variation of differential gain with carrier confinement energy, which is required as an input to the calculations, was theoretically calculated considering valence band mixing effects. This calculation also considered carrier occupation in the SCH region under bandfilling and carrier overflow effects.

MQW lasers have lower wavelength chirp under modulation *only* in the case where the carrier transport effects are severe, and the contribution of the carrier confinement regions to the total index change with change in carrier density is dominant. In general, when the carrier transport effects are minimal, the variation of wavelength chirp with the number of quantum wells is somewhat more complicated. This is because the increase in the optical confinement factor is not linear in the number of quantum wells, and due to gain saturation in quantum well lasers, the increase in the differential gain for MQW lasers is not linear with the optical confinement factor.

## Journal Publications

1. R. Nagarajan, T. Fukushima, J. E. Bowers, R. S. Geels, and L. A. Coldren, "High Speed InGaAs/GaAs Strained Multiple Quantum Well Lasers with Low Damping," *Appl. Phys. Lett.*, vol. 58, no. 21, pp. 2326-2328, May 1991.
2. R. Nagarajan, T. Fukushima, J. E. Bowers, R. S. Geels, and L. A. Coldren, "Single Quantum Well Strained InGaAs/GaAs Lasers with Large Modulation Bandwidth and Low Damping," *Electron. Lett.*, vol. 27, no. 12, pp. 1058-1060, June 1991.
3. T. Fukushima, R. Nagarajan, J. E. Bowers, R. A. Logan, and T. Tanbun-Ek, "Relative Intensity Noise Reduction in InGaAs/InP Multiple Quantum Well Lasers with Low Nonlinear Damping," *IEEE Photon. Tech. Lett.*, vol. 3, no. 8, pp. 691-693, September 1991.
4. R. Nagarajan, T. Fukushima, S. W. Corzine, and J. E. Bowers, "Effects of Carrier Transport on High Speed Quantum Well Lasers," *Appl. Phys. Lett.*, vol. 59, no. 15, pp. 1835-1837, October 1991.
5. R. Nagarajan, T. Fukushima, M. Ishikawa, J. E. Bowers, R. S. Geels, and L. A. Coldren, "Transport Limits in High Speed Quantum Well Lasers: Experiment and Theory," *IEEE Photon. Tech. Lett.*, vol. 4, no. 2, pp. 121-123, February 1992.
6. R. Nagarajan, M. Ishikawa, and J. E. Bowers, "Effects of Carrier Transport on Relative Intensity Noise and Critique of K Factor Prediction of Modulation Response," *Electron. Lett.*, vol. 28, no. 9, pp. 846-847, April 1992.
7. M. Ishikawa, T. Fukushima, R. Nagarajan, and J. E. Bowers, "Temperature Dependence of Damping in High Speed Quantum Well Lasers," *Appl. Phys. Lett.*, vol. 61, no. 4, pp. 396-398, July 1992.
8. R. Nagarajan, R. P. Mirin, T. E. Reynolds, and J. E. Bowers, "Effect of the Confinement Layer Composition on the Internal Quantum Efficiency and Modulation Response of Quantum Well Lasers," *IEEE Photon. Tech. Lett.*, vol. 4, no. 8, pp. 832-834, August 1992.
9. R. Nagarajan, M. Ishikawa, T. Fukushima, R. S. Geels, and J. E. Bowers, "High Speed Quantum Well Lasers and Carrier Transport Effects," *IEEE J. Quantum Electron.*, vol. 28, no. 10, pp. 1990-2008, October 1992.
10. M. Ishikawa, R. Nagarajan, T. Fukushima, J. Wasserbauer, and J. E. Bowers, "Long Wavelength High Speed Semiconductor Lasers with Carrier Transport Effects," *IEEE J. Quantum Electron.*, vol. 28, no. 10, pp. 2230-2241, October 1992.

11. R. Nagarajan, "Carrier Transport Effects in High Speed Quantum Well Lasers," Ph.D. Dissertation submitted to the Department of Electrical and Computer Engineering, University of California, Santa Barbara, July 1992 (unpublished).
12. T. Fukushima, R. Nagarajan, M. Ishikawa, and J. E. Bowers, "High-Speed Dynamics in InP based Multiple Quantum Well Lasers," *Jpn. J. Appl. Phys.*, vol. 32, Pt. 1, no. 1A, pp. 89-102, January 1993.
13. R. Nagarajan, and J. E. Bowers, "Effects of Carrier Transport on Injection Efficiency and Wavelength Chirping in Quantum Well Lasers," submitted to *IEEE J. Quantum Electron.*

### Conference Presentations

1. R. Nagarajan, T. Fukushima, J. Bowers, R. Geels, and L. Coldren, "High Speed InGaAs/GaAs Strained Multiple Quantum Well Ridge Waveguide Lasers with Low Damping," *Conference on Optical Fiber Communication (OFC) '91*, paper PD8, San Diego, USA, February 1991.
2. R. Nagarajan, T. Fukushima, and J. Bowers, "High Speed and Noise Properties of Strained InGaAs/GaAs Multiple Quantum Well Lasers," *Engineering Foundation Conference on High Speed/High Frequency Optoelectronics*, Palm Coast (Florida), USA, March 1991.
3. R. Nagarajan, T. Fukushima, J. E. Bowers, R. S. Geels, and L. A. Coldren, "Comparison of Modulation and Noise Properties of Strained InGaAs and Unstrained GaAs Single Quantum Well Lasers," *Conference on Lasers and Electro-Optics (CLEO) '91*, paper CTuK1, Baltimore, USA, May 1991.
4. R. Nagarajan, T. Fukushima, J. E. Bowers, R. S. Geels, and L. A. Coldren, "High Speed Single Quantum Well InGaAs/GaAs Laser Design and Experiment," *Device Research Conference '91*, paper IIA-1, Boulder, USA, June 1991.
5. R. Nagarajan, T. Fukushima, J. E. Bowers, R. S. Geels, and L. A. Coldren, "High Speed Single Quantum Well Strained InGaAs/GaAs Lasers," *17th European Conference on Optical Communication (ECOC) '91/18th International Conference on Integrated Optics and Optical Fiber Communication (IOOC) '91*, paper Tu.A4.3, Paris, France, September 1991.
6. R. Nagarajan, T. Fukushima, J. E. Bowers, R. S. Geels, and L. A. Coldren, "High Speed Strained InGaAs/GaAs Quantum Well Lasers," *Government Microcircuit Applications Conference (GOMAC) '91*, paper 10.7, Orlando, USA, November 1991.

7. M. Ishikawa, T. Fukushima, R. Nagarajan, and J. E. Bowers, "Temperature Dependence of Damping in High Speed Quantum Well Lasers," *Optical Society of America (OSA) Annual Meeting*, paper TuHH4, San Jose, USA, November 1991.
8. R. Nagarajan, M. Ishikawa, T. Fukushima, R. S. Geels and J. E. Bowers, "Carrier Transport Effects in High-Speed Quantum-Well Lasers," *Laser Diode Technology and Applications IV, OE/LASE '92 (SPIE Conference #1634)*, paper 1634-14, Los Angeles, USA, January 1992.
9. R. Nagarajan, T. Fukushima, M. Ishikawa, J. E. Bowers, R. S. Geels, and L. A. Coldren, "Transport Limits in High Speed Quantum Well Lasers," *Conference on Optical Fiber Communication (OFC) '92*, paper ThB5, San Jose, USA, February 1992.
10. R. Nagarajan, and J. E. Bowers, "Carrier Transport in High Speed Quantum Well Lasers," *Workshop on Compound Semiconductor Materials and Devices (WOCSEMMAD) '92*, San Antonio, USA, February 1992.
11. R. Nagarajan, M. Ishikawa and J. E. Bowers, "Effects of Carrier Transport on Relative Intensity Noise and Modulation Response in Quantum Well Lasers," *High-Speed Electronics and Optoelectronics, Symposium on Compound Semiconductor Physics and Devices (SPIE Conference #1680)*, paper 1680-11, Somerset (New Jersey), USA, March 1992.
12. R. Nagarajan, and J. E. Bowers, "Effects of Bandfilling and Thermionic Emission on the Modulation Response of Quantum Well Lasers," *Engineering Foundation Conference on High Speed Optoelectronic Devices and Circuits II*, Banff (Alberta), Canada, August 1992.
13. R. Nagarajan, R. P. Mirin, T. E. Reynolds, and J. E. Bowers, "Carrier Confinement and its Effect on the Internal Quantum Efficiency and Modulation Response of Quantum Well Lasers," *13th International Semiconductor Laser Conference*, paper F-3, Takamatsu, Japan, September 1992.
14. R. Nagarajan, "Carrier Transport Effects in High Speed Quantum Well Lasers," *Ultrafast Electronics & Optoelectronics '93*, paper MA2 (Invited), San Francisco, USA, January 1993.
15. J. Bowers, R. Nagarajan, and T. Ishikawa, "Picosecond Carrier Transport in Quantum Well Lasers," *Quantum Electronics and Laser Science Conference (QELS) '93*, paper (Invited), Baltimore, USA, May 1993.

Wafer #	# QWs	SCH Comp.	$L_s$ (Å)	$L_w$ (Å)	$\Gamma$ (%)	Min. $J_{th}$ (A/cm <sup>2</sup> )	$\alpha_{int}$ (cm <sup>-1</sup> )	$\eta_i$ (%)
A	1	Al <sub>0.1</sub> Ga <sub>0.9</sub> As	760	80	2.9	140	21.8	95.5
B	1	Al <sub>0.1</sub> Ga <sub>0.9</sub> As	1500	80	2.7	129	11.8	80.7
C	1	Al <sub>0.1</sub> Ga <sub>0.9</sub> As	3000	80	1.9	93	4.3	83.5
D	3	Al <sub>0.15</sub> Ga <sub>0.85</sub> As	710	70	8.2	322	59.2	90.7
E	3	GaAs	710	70	8.9	387	36.9	66.7
F	1	Al <sub>0.1</sub> Ga <sub>0.9</sub> As	900	80	3.0	125	6.9	93.8
G	3	Al <sub>0.1</sub> Ga <sub>0.9</sub> As	700	80	9.2	247	14.4	83.8

$L_s$	Width of one side of SCH layer	$L_w$	Width of quantum well
$\Gamma$	Optical confinement factor	Min. $J_{th}$	Minimum threshold current density
$\alpha_{int}$	total internal loss	$\eta_i$	internal quantum efficiency
# QWs	Number of Quantum Wells	SCH Comp	SCH Composition

Table 1 Material quality of the wafers considered in this study.

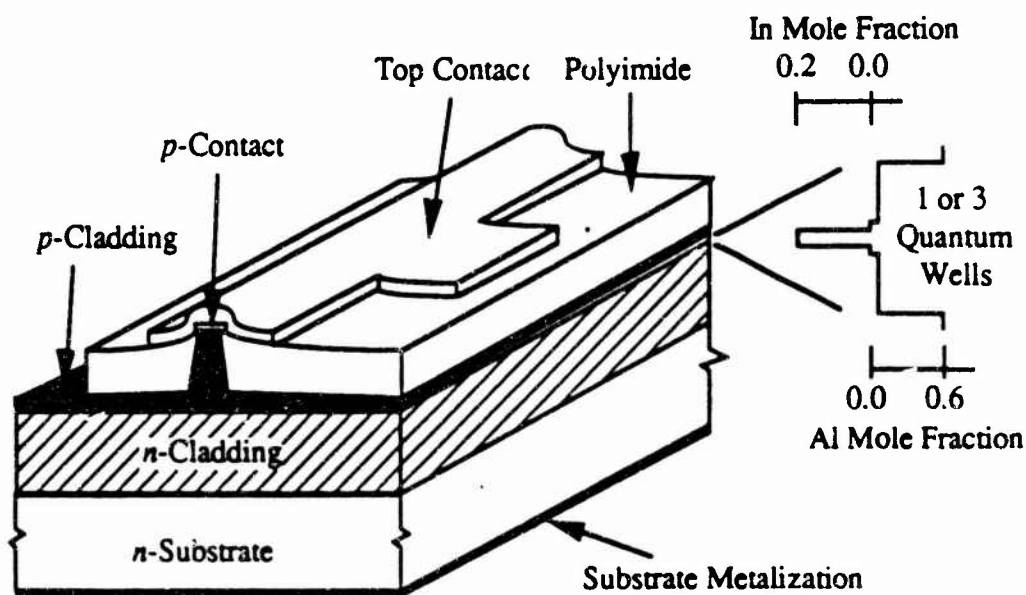


Fig. 1 Polyimide buried ridge waveguide laser.

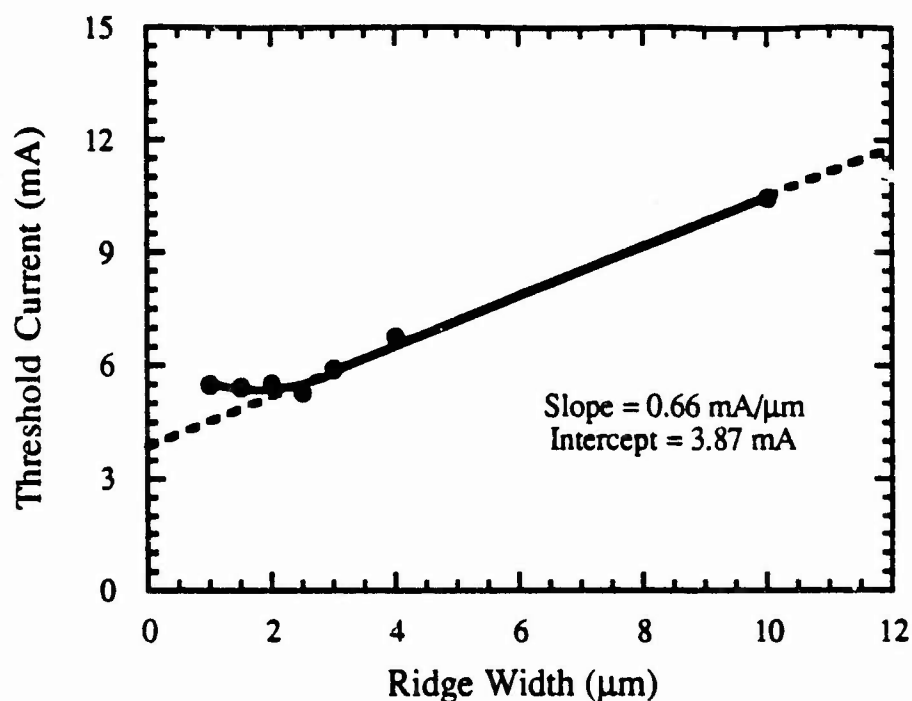


Fig. 2 Variation of threshold current with ridge width for  $170 \mu\text{m}$  cavity length 3 QW device (Sample G).

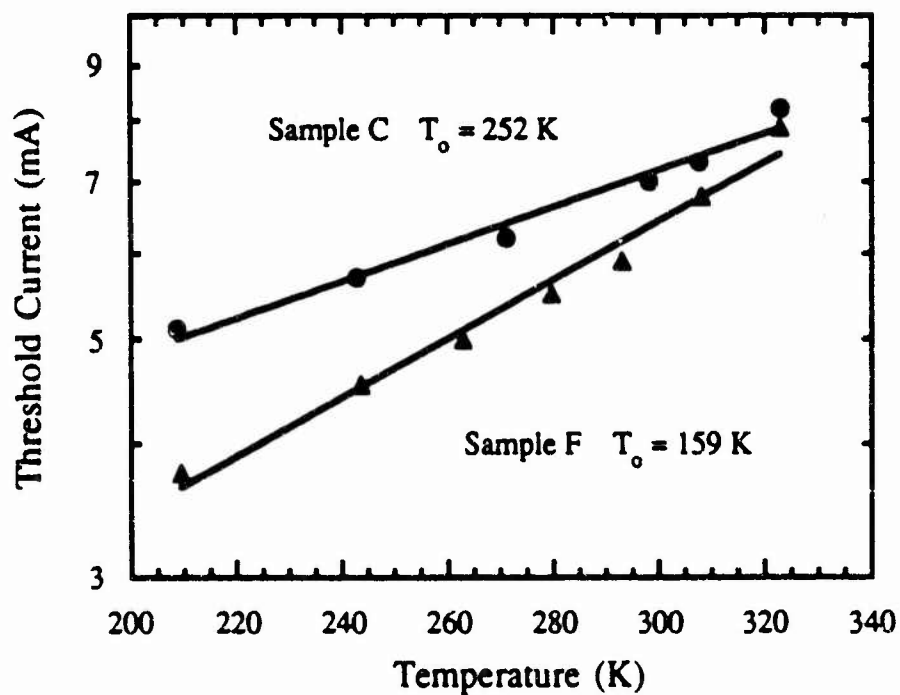


Fig. 3 Variation of threshold current with temperature for two SQW laser samples. Sample C has a  $300 \mu\text{m}$  long cavity and  $2.5 \mu\text{m}$  wide ridge. Sample F has a  $200 \mu\text{m}$  long cavity and  $2.0 \mu\text{m}$  wide ridge.



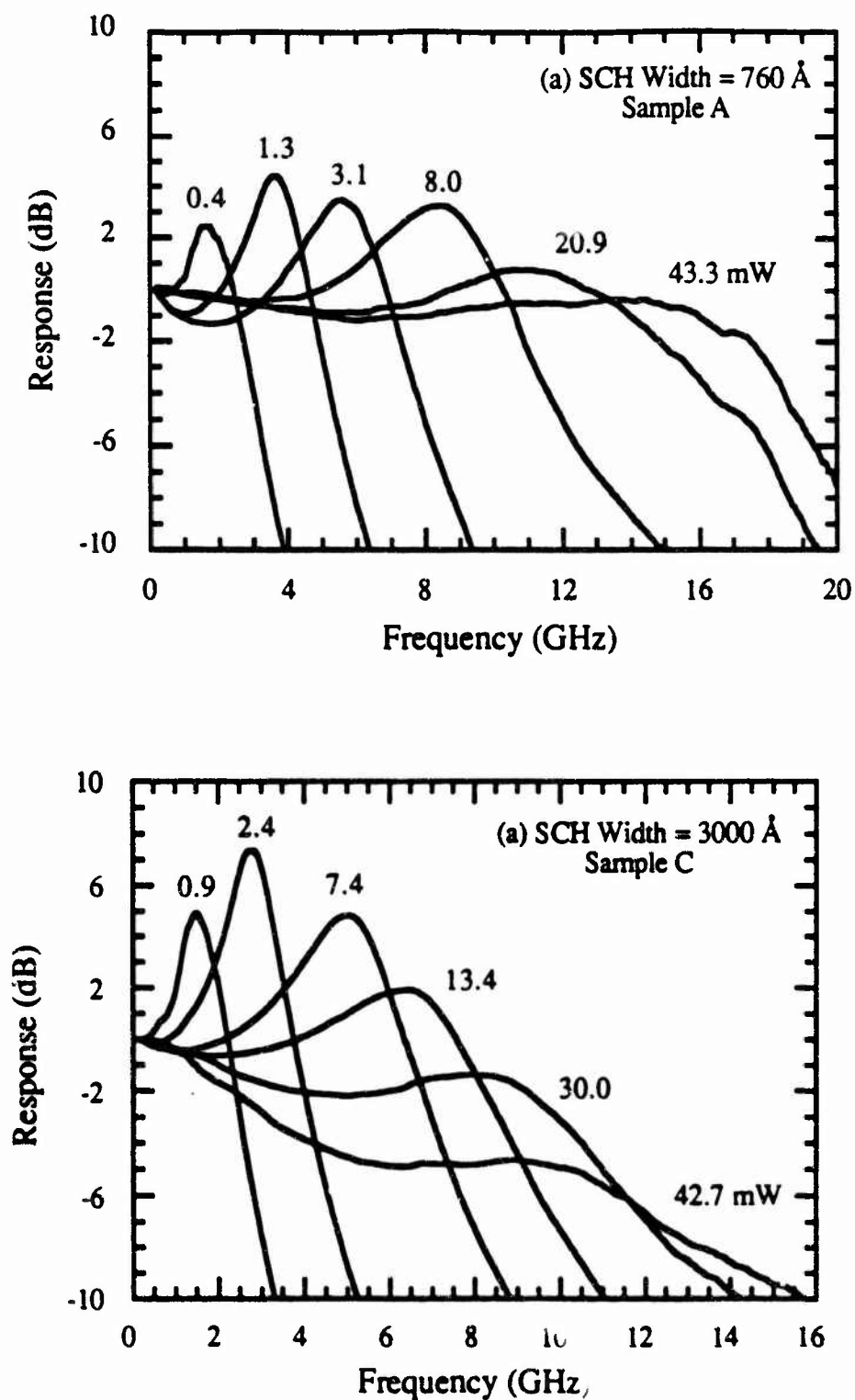


Fig. 4 C.W. modulation response for the narrow SCH Sample A, compared to the wide SCH Sample C. The significant rolloff in the modulation response and the shift in the position of the resonance peak to lower frequencies at comparable powers in Sample C is due to the carrier transport across the SCH region.

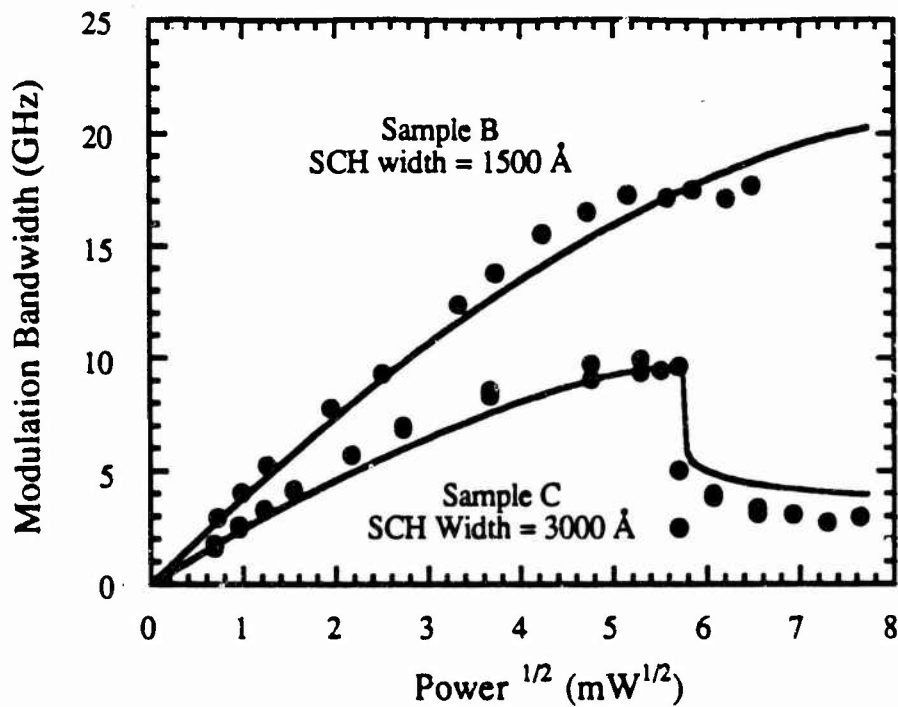


Fig. 5 Comparison of the carrier transport model and experiment for the variation of modulation bandwidth with the square root of power.

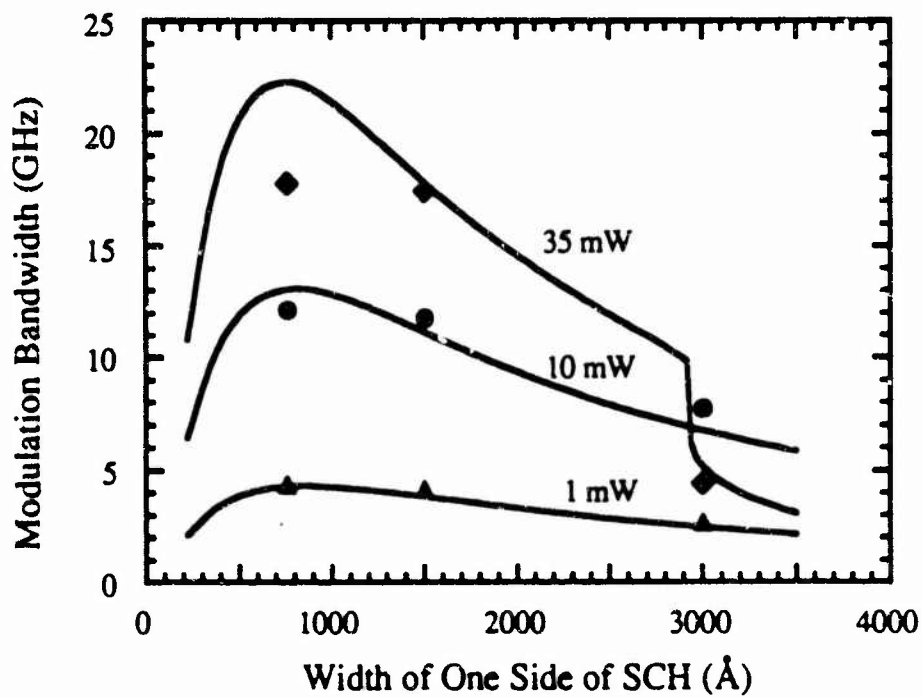


Fig. 6 Comparison of the calculated and measured variation in modulation bandwidth with SCH width.

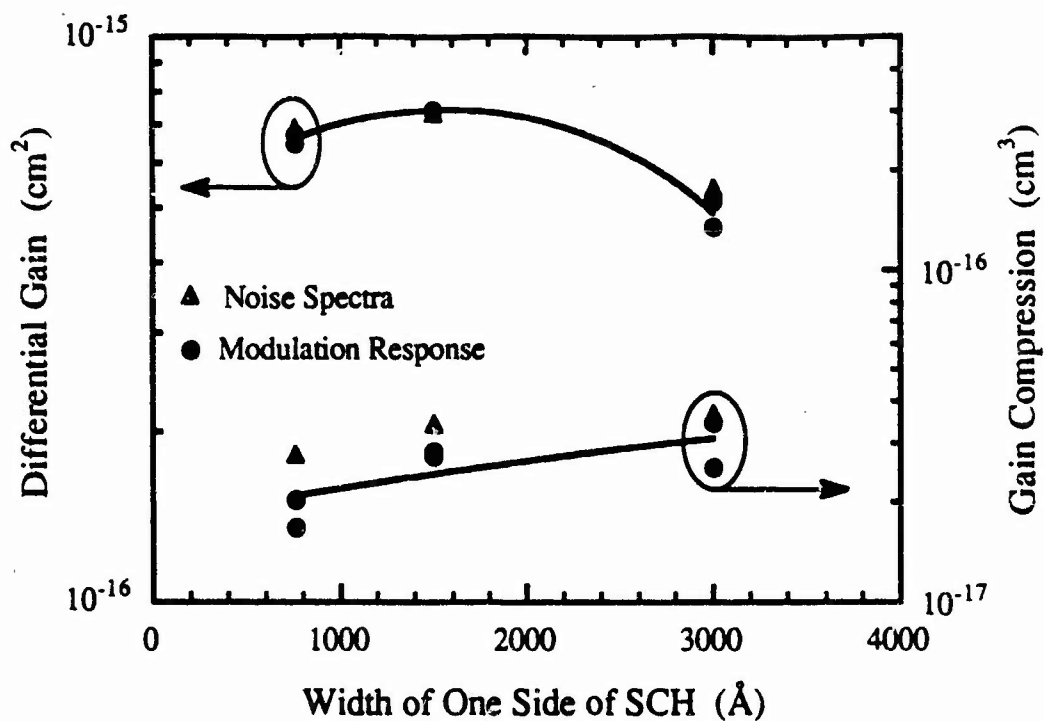


Fig. 7 Differential gain and gain compression factor determined from the modulation response and noise spectra.

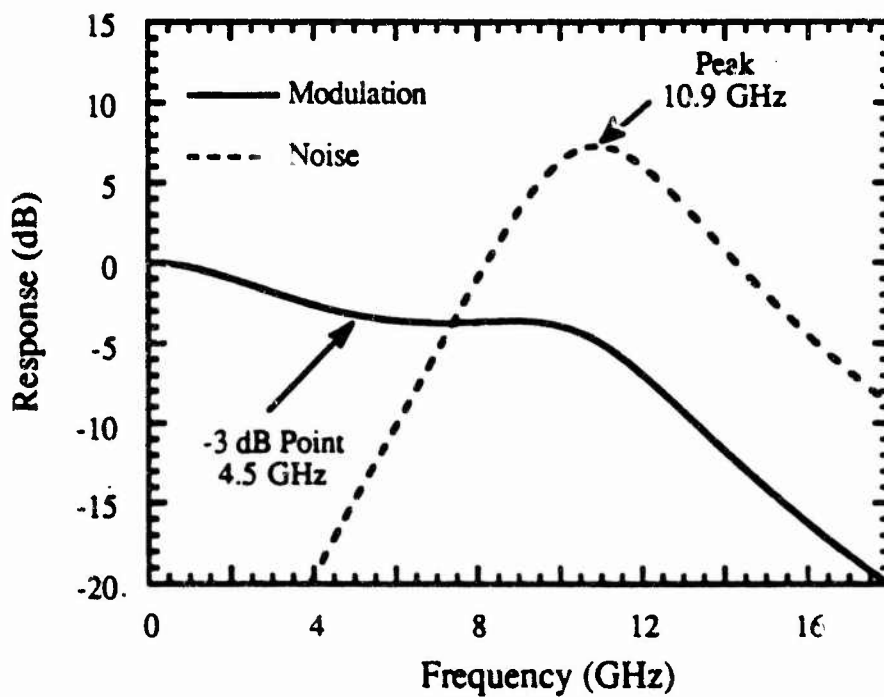


Fig. 8 Comparison of the noise spectrum and the modulation response for the same device parameters. The noise spectrum indicates a much larger modulation bandwidth than is physically possible.

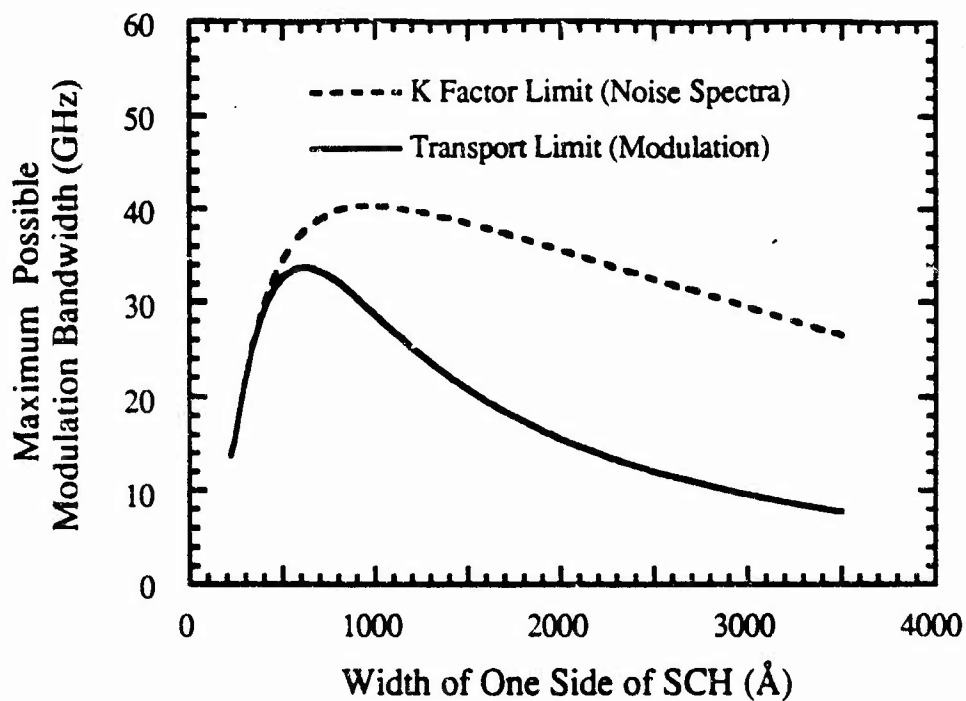


Fig. 9 Comparison of maximum possible modulation bandwidth inferred from the modulation response and intensity noise measurements.

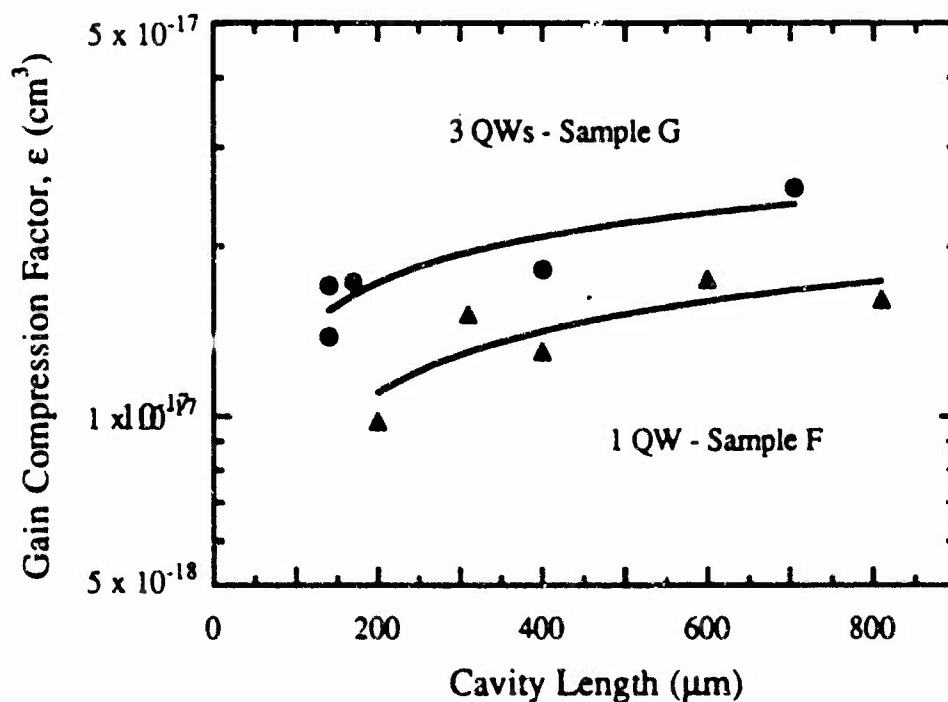


Fig. 10 Variation of the gain compression factor with cavity length for MQW and SQW lasers.

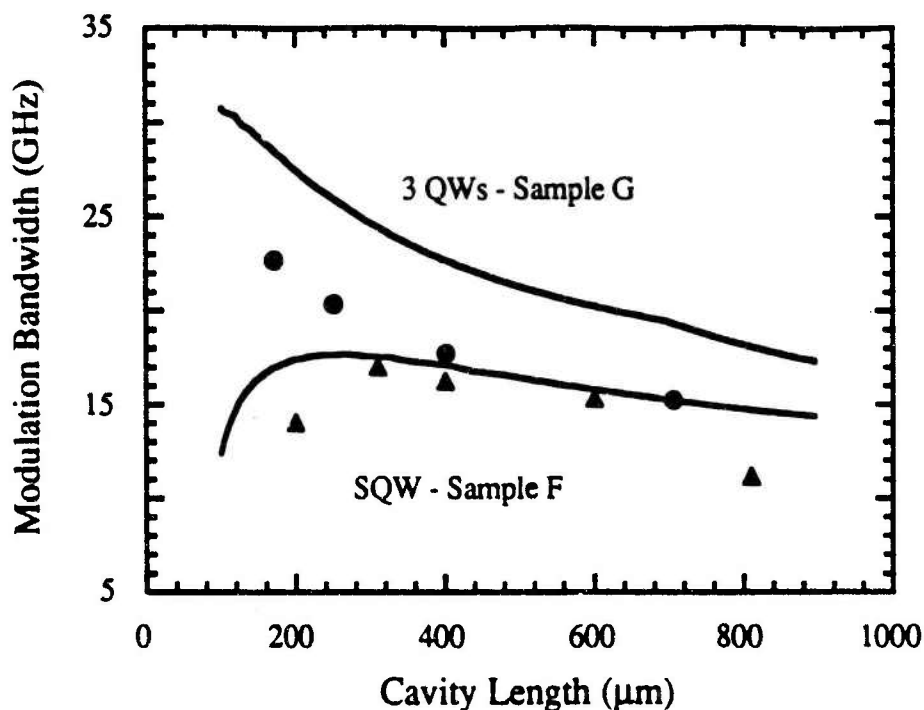


Fig. 11 Comparison of the calculated and measured variation in modulation bandwidth with cavity length for SQW and MQW lasers.

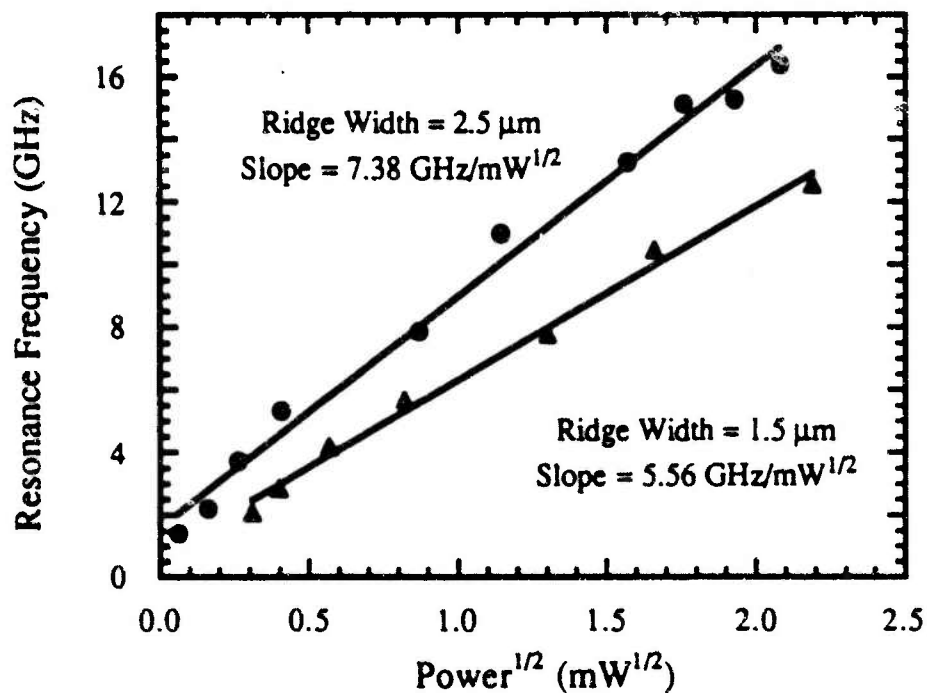


Fig. 12 Variation of resonance frequency with square root of power for two 150  $\mu\text{m}$  cavity length 3 QW devices (Sample D) with different ridge widths.

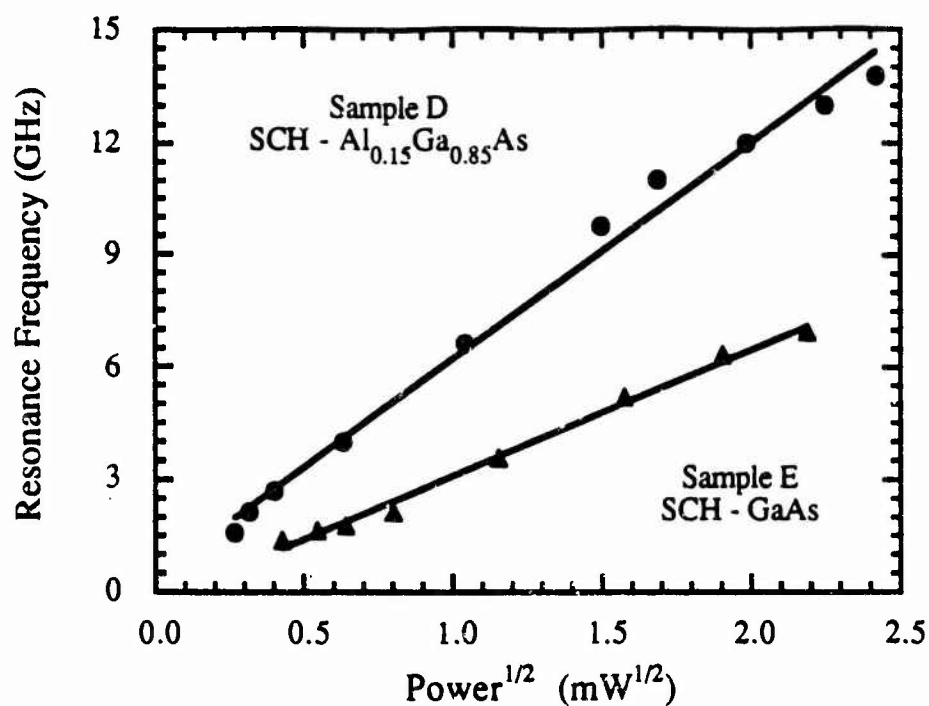


Fig. 13 Dependence of the resonance frequency on the square root of power for the MQW samples with a higher (Al<sub>0.15</sub>Ga<sub>0.85</sub>As) and lower (GaAs) energy barrier in the SCH.

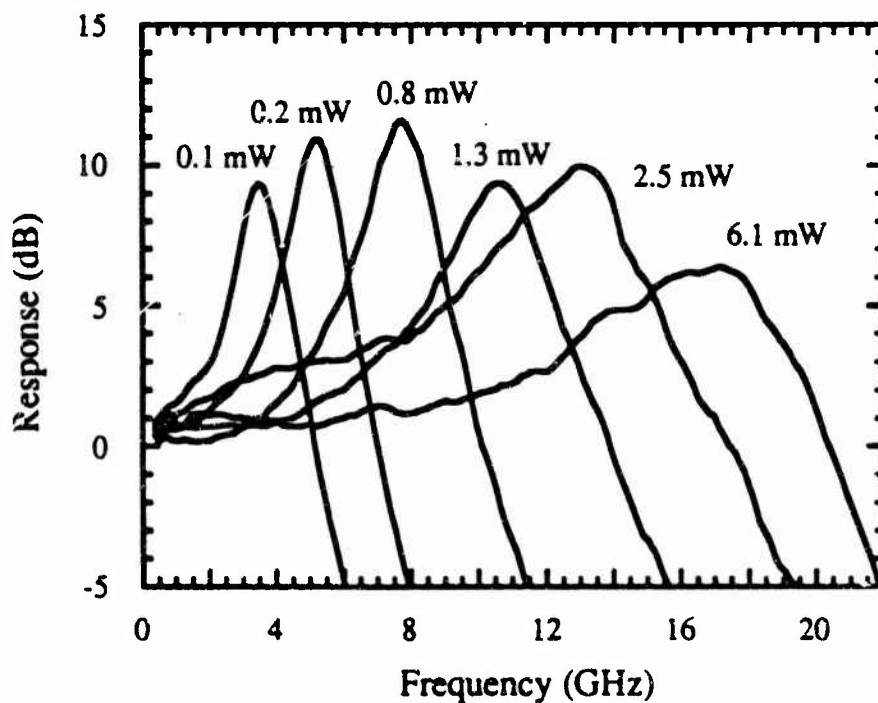


Fig. 14 Modulation response for a 3 QW sample with 150  $\mu\text{m}$  cavity length, 2.5  $\mu\text{m}$  ridge width and Al<sub>0.15</sub>Ga<sub>0.85</sub>As SCH.

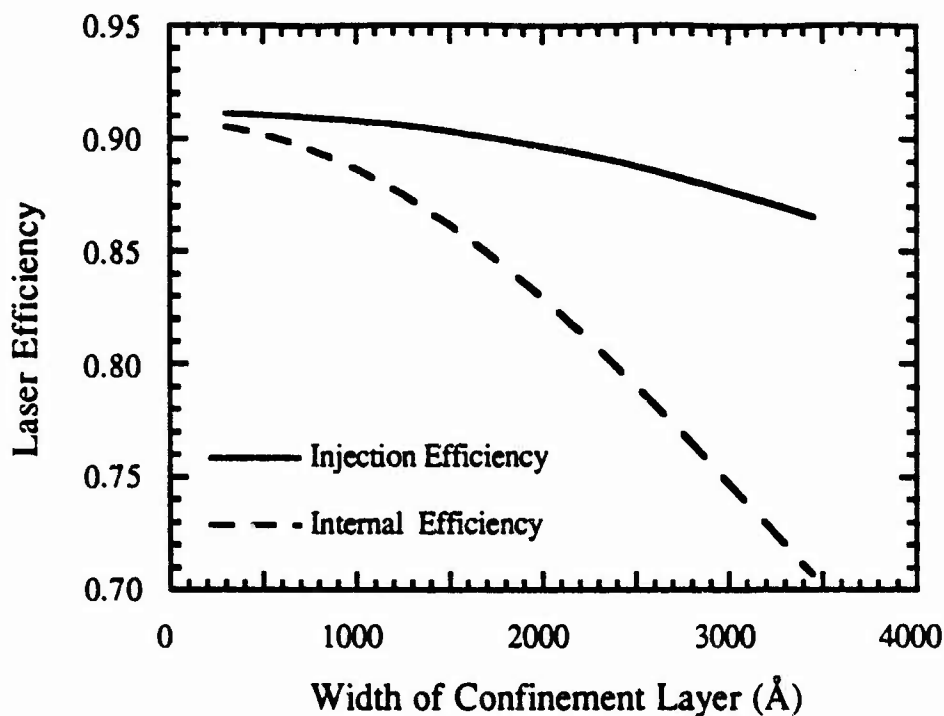


Fig. 15 Variation of the laser internal and injection efficiencies as a function of the SCH width. The calculation is done for a SQW structure with a 80 Å well width and a 10% Al mole fraction in the SCH.

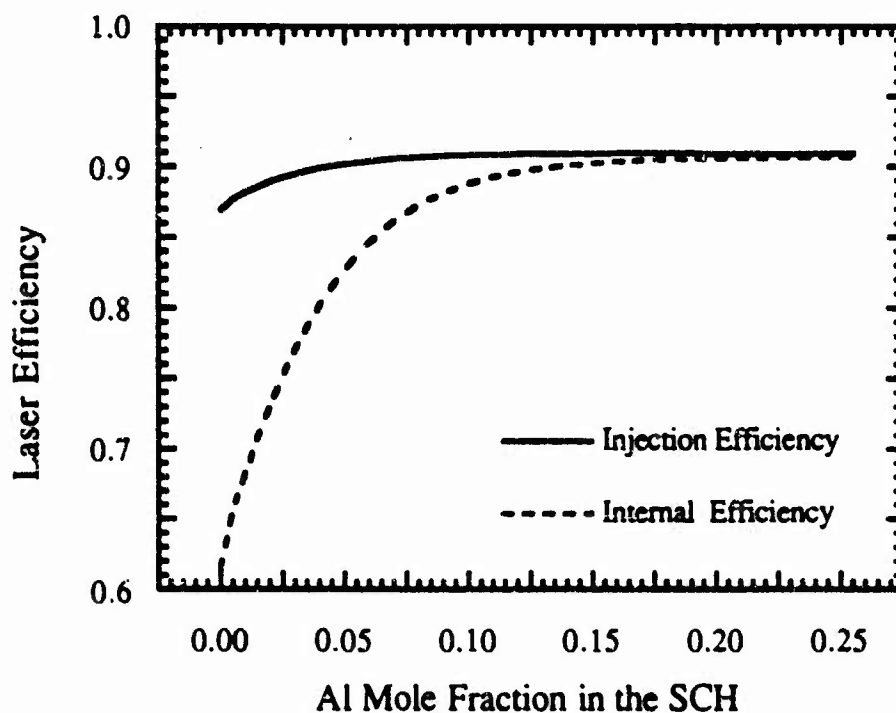


Fig. 16 Variation of the laser internal and injection efficiencies with carrier confinement energy in the SCH. The calculation is also done for a SQW structure with a 1000 Å wide SCH.

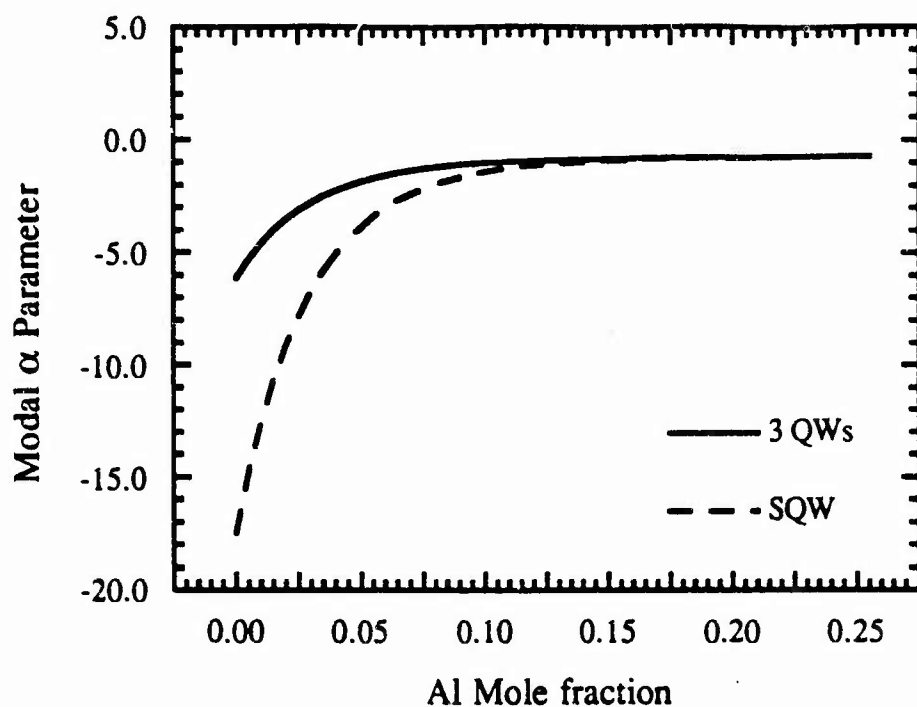


Fig. 17 Variation of the modal  $\alpha$  parameter with carrier confinement energy in the SCH for SQW and MQW laser structures. The calculation is done for a 1000 Å wide SCH.

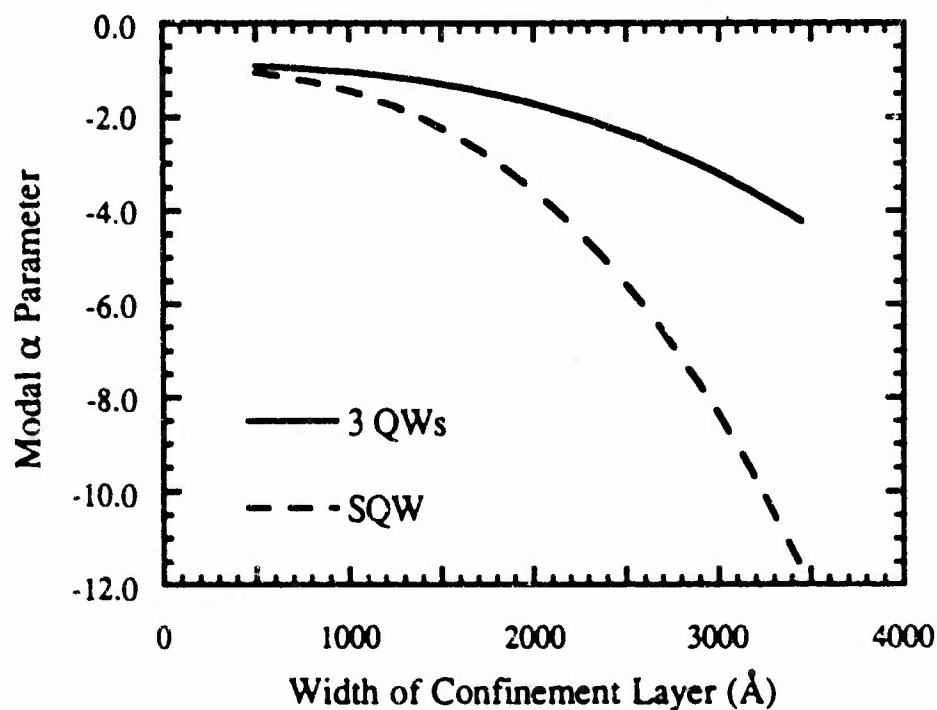


Fig. 18 Variation of the modal  $\alpha$  parameter as a function of the SCH width for SQW and MQW laser structures. The calculation is done for 10% Al mole fraction in the SCH.



## **SECTION 3**

**MBE Growth of (Al,Ga,In)As Strained Quantum Well Lasers on InP**

### 3.1 Introduction

The conduction band offset of the (Al,In)As/(Ga,In)As lattice matched to InP is 0.5 eV, relatively large compared to the 0.22 eV of the InP/(Ga,In)As heterojunction. A large conduction band offset is advantageous in quantum well lasers for confining the light effective mass electrons. Also, the all-arsenide (Al,Ga,In)As system can be grown directly on a InP substrate by conventional solid source molecular beam epitaxy (MBE) with excellent thickness control and uniformity, which are favorable for the growth of thin ( $<100 \text{ \AA}$ ) quantum well structures. Motivated by the above advantages, we begun our work on (Al,Ga,In)As quantum well lasers on InP in the Fall of 1989. The following paragraphs give the highlights of our investigation, broken down into three sections: Material Growth and Characterization, Broad Area Laser Results, and Ridge Laser Results.

### 3.2 Material Growth and Characterization

Initially, efforts focused on optimizing the MBE growth of (Al,In)As and (Ga,In)As alloys on InP substrates. Precise and reproducible flux control ( $< \pm 3\%$ ) is required to grow device quality alloys ( $\Delta a/a < \pm 10^{-4}$ ) lattice matched to the InP substrate. In order to meet these stringent requirements, we coupled MBE in-situ reflection high energy electron diffraction (RHEED) measurements with post-growth high resolution x-ray diffraction (HRXD) measurements to determine optimal growth conditions. The RHEED measurements allow us, prior to the growth, to reproducibly measure the Group III flux rates which determine the subsequent alloy composition. Post-growth HRXD measurements enable us to correlate the flux measurements with resulting alloy composition. This technique of using RHEED in fine tuning the Group III fluxes has enabled us to routinely achieve lattice matching to  $\Delta a/a < \pm 10^{-4}$ .

Excellent optical properties were observed in lattice-matched ternary layers using low temperature 1.4 K photoluminescence (PL). As shown in Fig. 1, a respectable FWHM of 4.1 meV for (Ga,In)As was measured. For (Al,In)As layers, FWHMs of 13 meV are observed which is relatively narrow compared to the literature values for this alloy. Quantum well structures for PL study have been grown as shown in Fig. 2. As can be seen in Fig. 3, state-of-the-art FWHMs are observed for the 540 °C substrate temperature, disregarding the 140 Å well due to lack of a superlattice buffer.

In order to optimize the waveguide design of a laser, knowledge of the refractive index is a necessity. However, prior to our work, little data existed on the refractive index data of the

(Al,Ga,In)As system in the literature. Hence, we undertook the task of determining the wavelength and compositional dependence of the refractive index of the (Al,Ga,In)As system. We used a reflection interference technique which extracts the refractive index difference between an single epilayer, i.e. (Al,Ga,In)As layer and its underlying InP substrate. Growing a number of samples of various compositions via our RHEED calibration technique, we were able to measure the refractive index difference relative to the well-known InP index. As shown in Fig. 4, the index of (Al,Ga,In)As is actually greater than that of InP, contrary to what would be expected from traditional bandgap relationships. The data shows a reasonable trend between the (Ga,In)As and (Al,In)As endpoints and has been empirically fitted as a function of wavelength and composition. This data enabled us to design optimal waveguide structures for separate confinement lasers as described in the next section.

### 3.3 Broad Area Laser Results

The use of strained quantum wells, both ternary and quaternary, have yielded state-of-the-art results with respect to threshold current density and internal losses at 1.55  $\mu\text{m}$ . Using the waveguiding structure in shown in Fig. 5, we have fabricated 50  $\mu\text{m}$  wide mesa etched broad area lasers. The etched mesa helps to minimize current spreading effects due to the top cladding and cap layers which obscure comparisons between different laser structures. Two different active regions were used in this study shown in Fig. 6. One active region was a homogenous ternary alloy of (Ga,In)As with three 35  $\text{\AA}$  wells. The other active region consisted of three 100  $\text{\AA}$  (Al,Ga,In)As quantum wells. The quaternary well material allows an extra degree of design freedom since the well width and layer strain can be varied while maintaining a 1.55  $\mu\text{m}$  transition energy. As can be seen in Fig. 7, both laser structures exhibited relatively low losses of  $<10 \text{ cm}^{-1}$ , better than previously reported for MBE grown (Al,Ga,In)As lasers. Threshold current densities as shown in Fig. 8 were also lower than any other MBE reports, with threshold current densities as low as 530  $\text{A/cm}^2$  measured for the strained quaternary laser. The reduced threshold current density resulting from the quaternary quantum well is attributed to improved carrier collection of the wider quantum well, evident from the larger injection efficiency  $\eta_i$ .

"Digital alloys" or short period superlattices of (Al,In)As/(Ga,In)As have been incorporated into laser structures. Digital alloys can improve composition control as well as minimize growth complexity of quaternary and graded layers for GRINSCH structures due to the elimination of source temperature changes. Using the GRINSCH structure in Fig. 9 with single and multiple quantum well active regions of homogenous (Al,Ga,In)As strained 100  $\text{\AA}$  quantum wells, broad area lasers were fabricated. Extremely low losses of 2 and 3  $\text{cm}^{-1}$  were observed as shown in Fig.

10, the best ever reported for (Al,Ga,In)As and very competitive to the best for any 1.55  $\mu\text{m}$  laser. The threshold current density as low as 290 A/cm<sup>2</sup> was measured for the single quantum well also a record low for MBE grown (Al,Ga,In)As as shown in Fig. 11. Interface smoothing and impurity trapping effects of the superlattice prior to the growth of the single quantum well are believed to be the key for achieving the record low threshold current density. Our previous attempts at single quantum well laser using homogenous alloys fail to lase. However, the three quantum well structure exhibited minimal improvement in threshold current density or differential quantum efficiency due to a reduction in the injection efficiency  $\eta_i$ . Enhanced superlattice recombination is speculated to be responsible for the degradation in carrier transport properties. Further investigation in evaluating the trade-off of the digital alloys is currently in progress.

### 3.4 Ridge Laser Results

Narrow ridge lasers have been fabricated from the homogenous alloy quaternary material using a polyimide isolation. The L-I of a 2x400  $\mu\text{m}$  ridge laser in Fig. 12 shows that the broad area results do scale with the reduced geometry with a threshold current of 20 mA and differential efficiency of 31% per facet observed. RIN measurements on the same device yielded the square root of output power versus resonance frequency plot in Fig. 13. From slope of the plot, we estimate a differential gain of  $2.9 \times 10^{-16} \text{ cm}^2$  for this non-optimized structure. Comparing this value of differential gain to other published three quantum well structures at 1.55  $\mu\text{m}$ , our value is comparable to the best reported for only three wells. Higher differential gains as well as resonance frequencies are expected for multiple quantum well strained (Al,Ga,In)As lasers which are optimized for high speed operation, i.e. 8-10 quantum wells.

We have developed a state-of-the-art technology for the MBE growth of (Al,Ga,In)As on InP. Device-quality (Al,Ga,In)As alloys can be controllably grown with excellent reproducibility. We have demonstrated record low threshold current densities and low waveguide losses at 1.55  $\mu\text{m}$  in broad area lasers grown by MBE using strained quaternary (Al,Ga,In)As quantum wells. Narrow ridge lasers operating CW at room temperature with threshold current as low as 20 mA have been measured. Although no high speed measurements were performed, RIN data suggest that high performance devices are possible using (Al,Ga,In)As strained quantum well in the active regions.

## Journal Publications

1. M. J. Mondry, D. I. Babic, J. E. Bowers, and L. A. Coldren, "Refractive Indexes of (Al,Ga,In)As Epilayers on InP for Optoelectronic Applications", *Photonic Tech. Lett.*, vol. 4, no. 6, pp. 627-630, June 1992.
2. M. J. Mondry, Z. M. Chuang, M. G. Peters, and L. A. Coldren, "Low Threshold Current Density 1.5  $\mu\text{m}$  (In,Ga,Al)As Quantum Well Lasers Grown by MBE", *Electronics Letters*, vol. 28, no. 15, pp. 1471-1472, July 1992.

## Conference Presentations

1. D. I. Babic, M. J. Mondry, L. A. Coldren, and J. E. Bowers, "Refractive Index of AlGaInAs on InP for Optoelectronic Applications", presented at LEOS Conf., San Jose, CA, OE9.6, November 1991.
2. M. J. Mondry, Z. M. Chuang, and L. A. Coldren, "Low Threshold Strained AlGaInAs Quantum Well Lasers on InP Grown by Molecular Beam Epitaxy", presented at Electronic Materials Conf., Cambridge, MA, S8, June 1992.

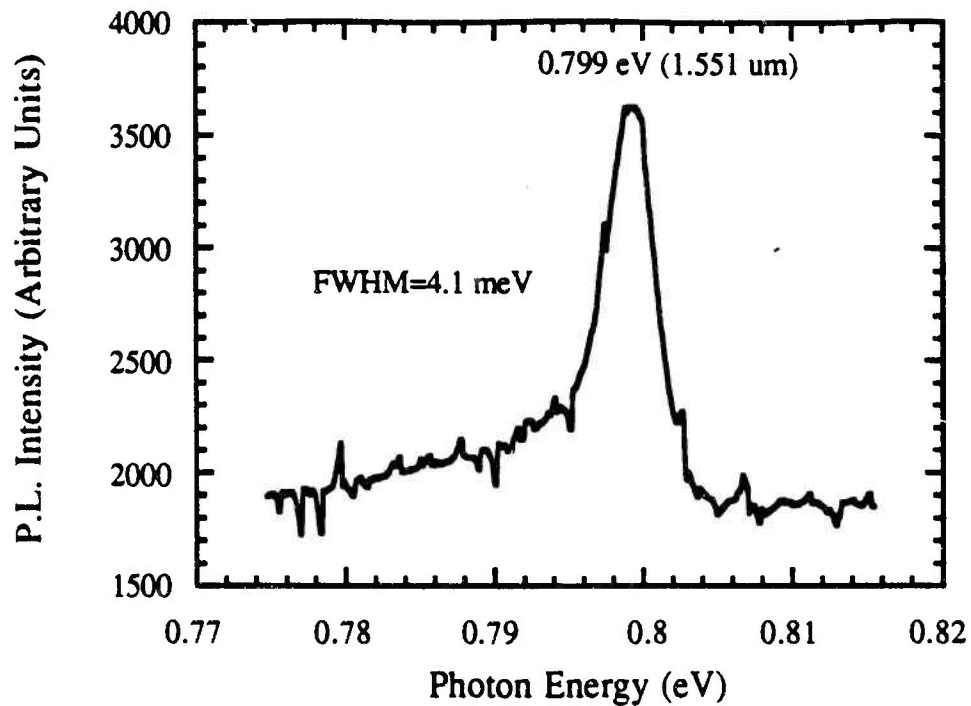


Fig. 1 1.4 K Photoluminescence of MBE grown (Ga,In)As epilayer on InP.

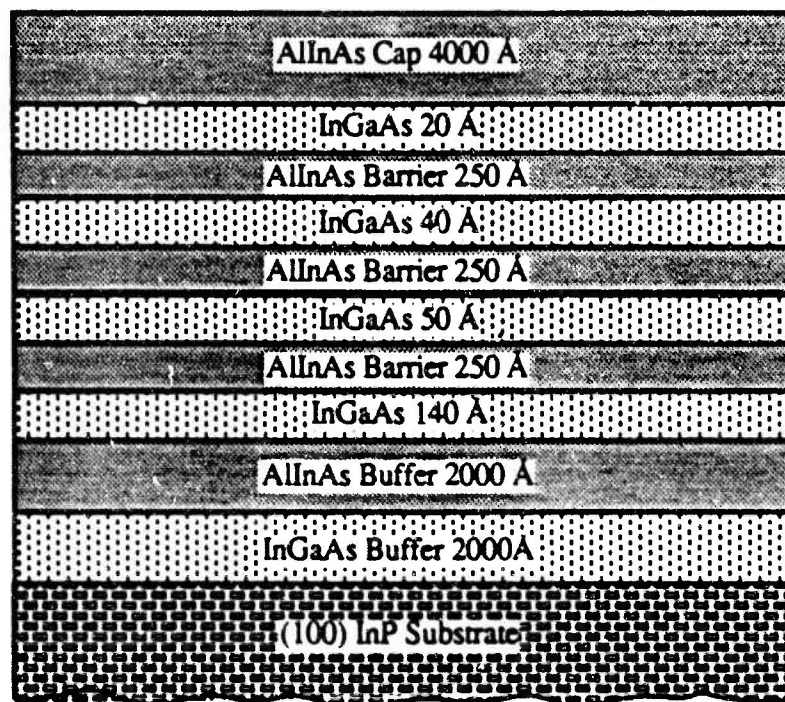


Fig. 2 Four (Ga,In)As quantum wells with (Al,In)As barriers grown at a substrate temperature of 540 °C.

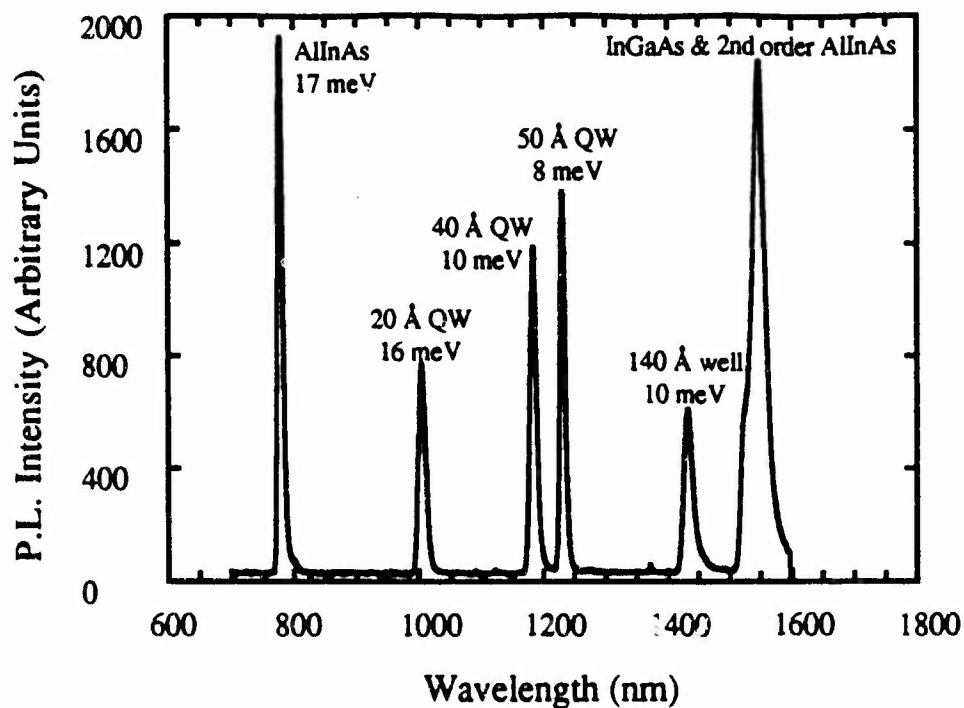


Fig. 3 1.4 K Photoluminescence from the quantum well structure of Fig. 2.

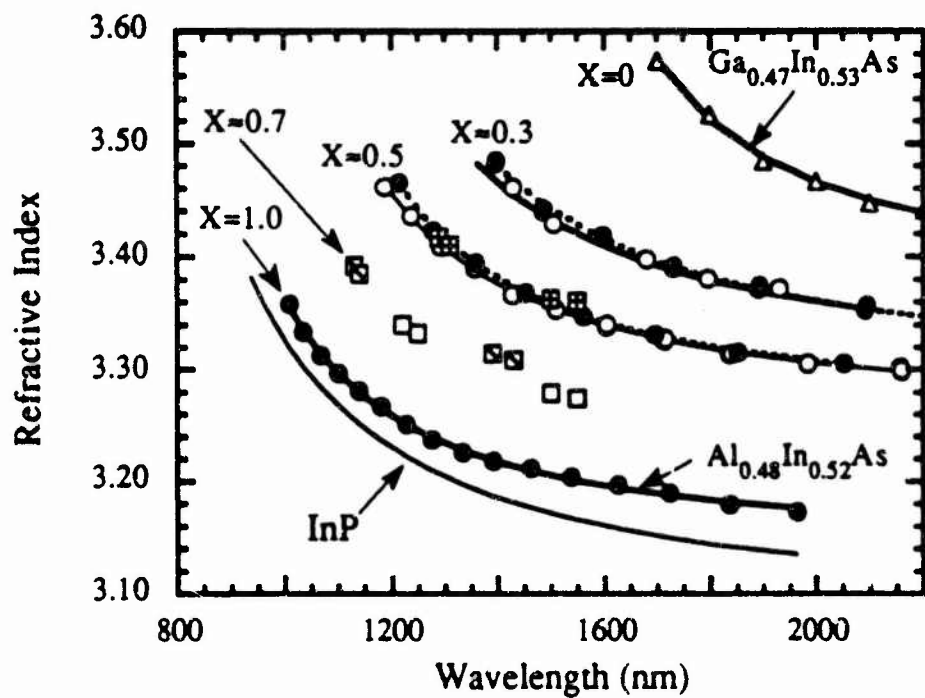


Fig. 4 Refractive indices of the quaternary alloy  $(\text{Al}_{0.48}\text{In}_{0.52}\text{As})_x(\text{Ga}_{0.47}\text{In}_{0.53}\text{As})_{1-x}$  as a function of wavelength and composition "X"

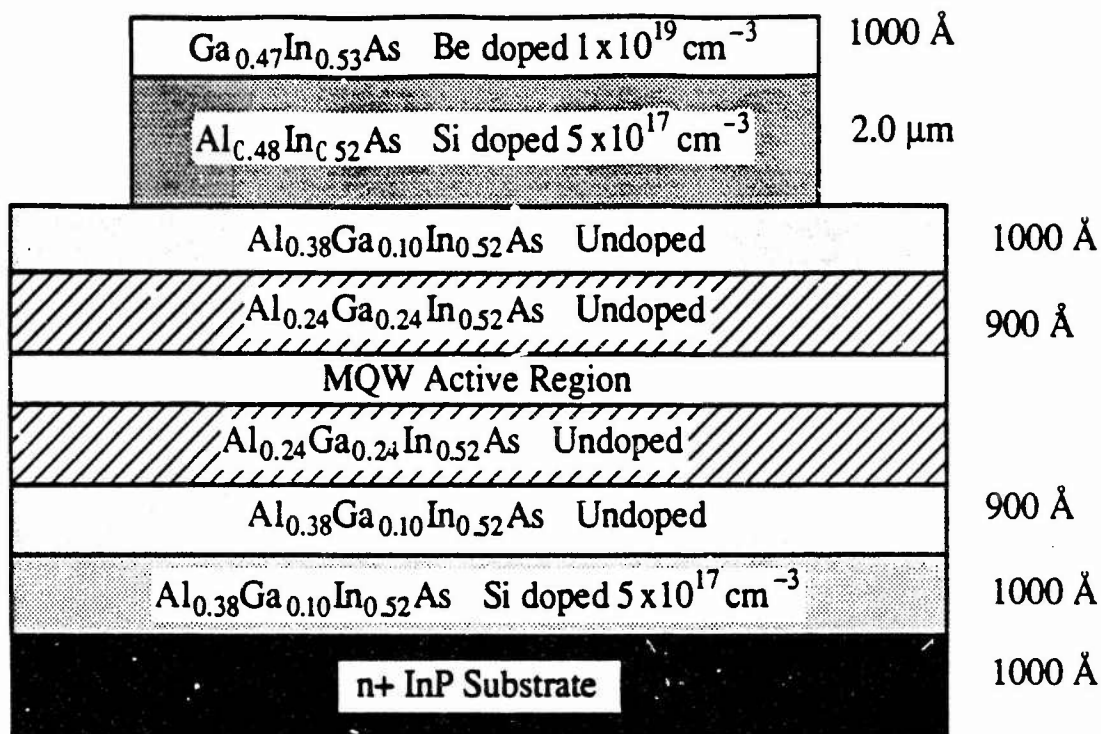


Fig. 5 Separate confinement laser structure using homogenous alloys for waveguiding regions. Active regions are detailed in Fig. 6.

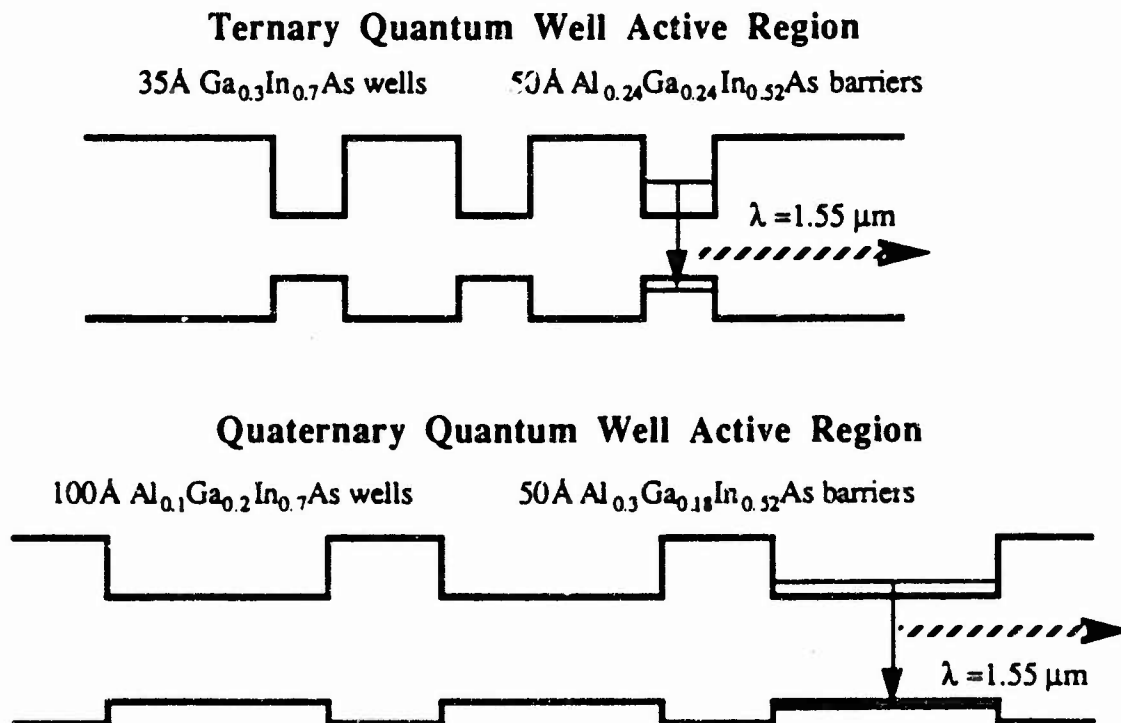


Fig. 6 Ternary and quaternary active regions used in laser structure of Fig. 5.



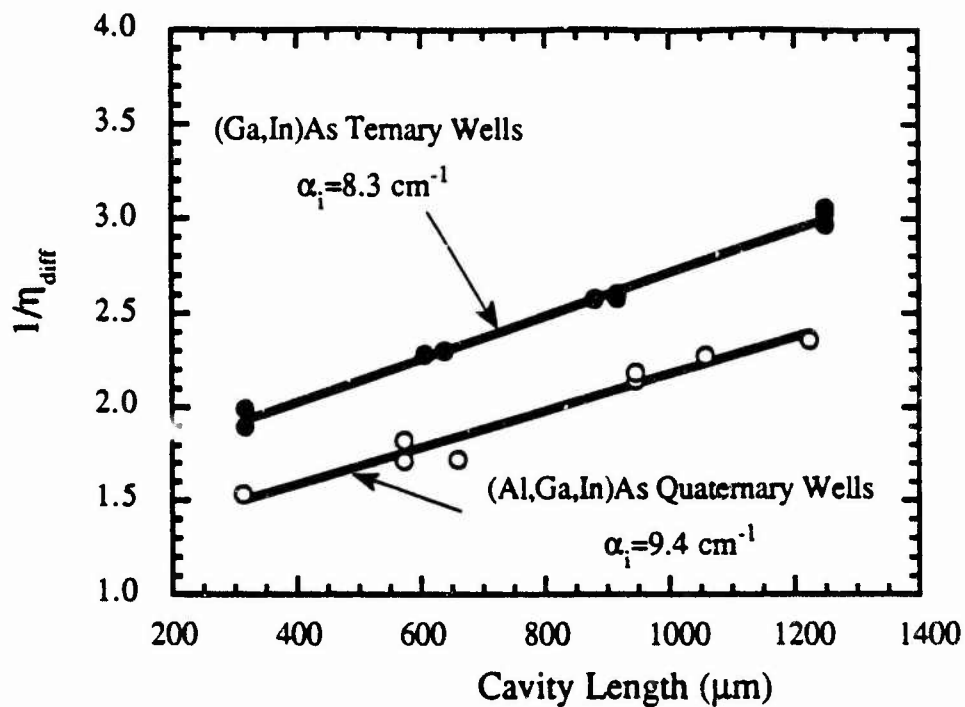


Fig. 7 Differential quantum efficiencies measured under pulsed conditions (600 ns at 10 kHz) at room temperature.

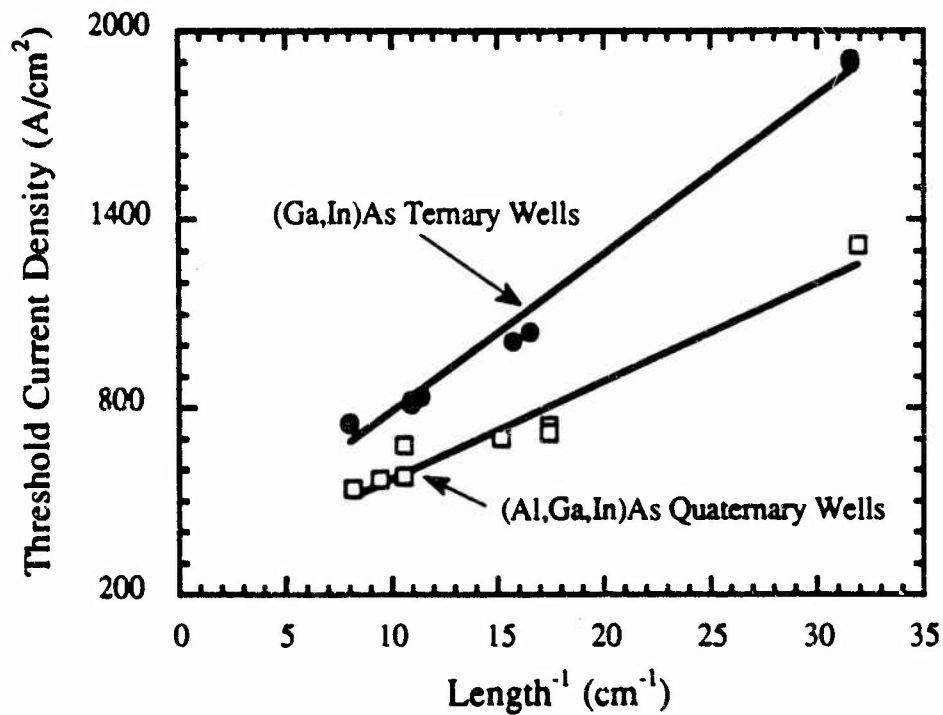


Fig. 8 Pulsed (600 ns at 10 kHz) threshold current densities measured at room temperature.

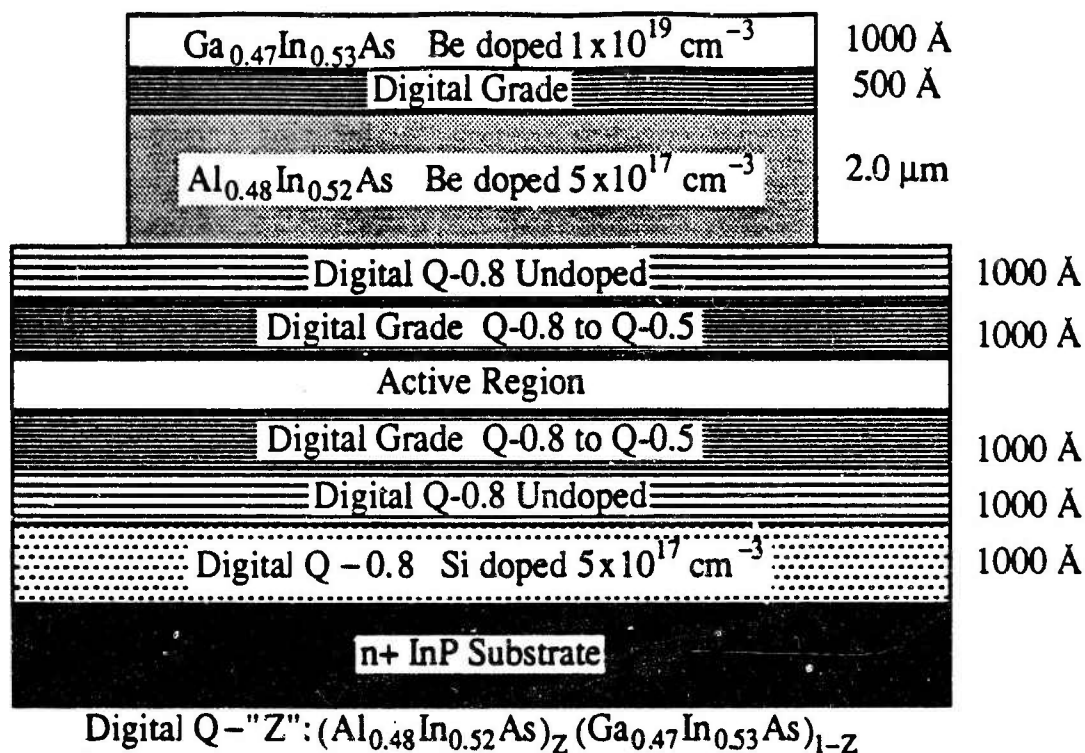


Fig. 9 "Digitally Graded" GRINSCH laser structure. Active region consisted of either a single or three 100 Å (Al,Ga,In)As strained quantum well(s).

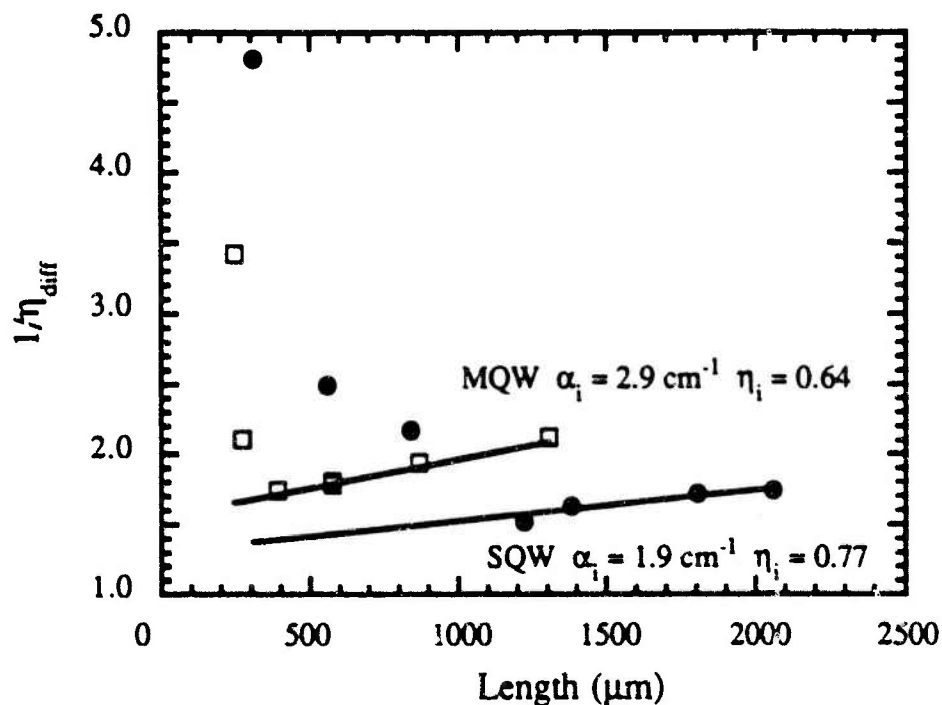


Fig. 10 Differential quantum efficiencies of "Digitally Graded" GRINSCH lasers measured under pulsed conditions (600 ns at 10 kHz) at room temperature.

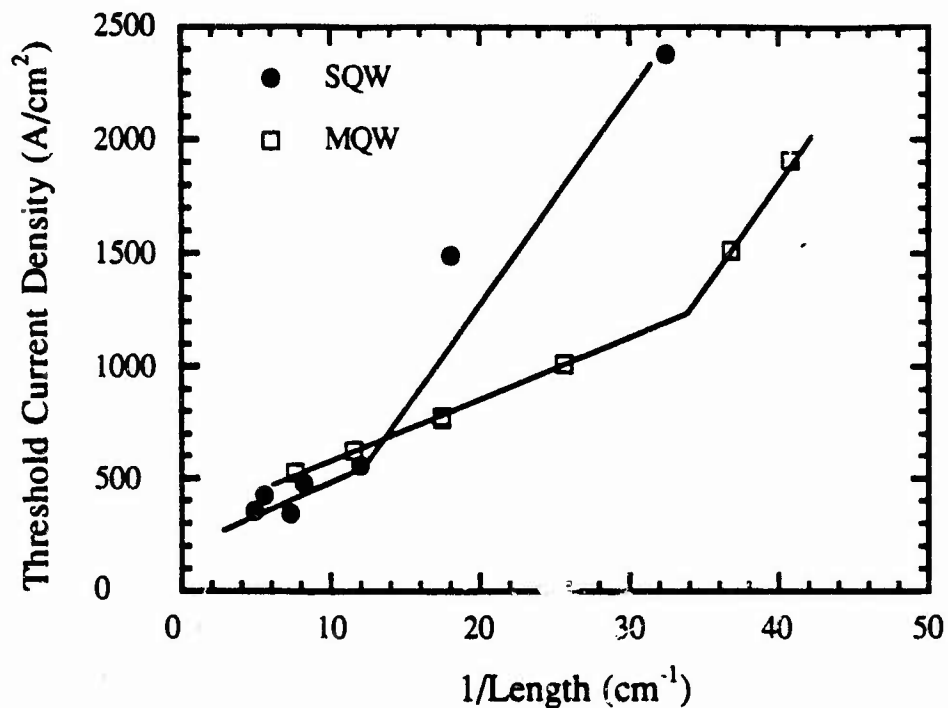


Fig. 11 Pulsed (600 ns at 10 kHz) threshold current densities of "Digitally Graded" GRINSCH lasers measured at room temperature.

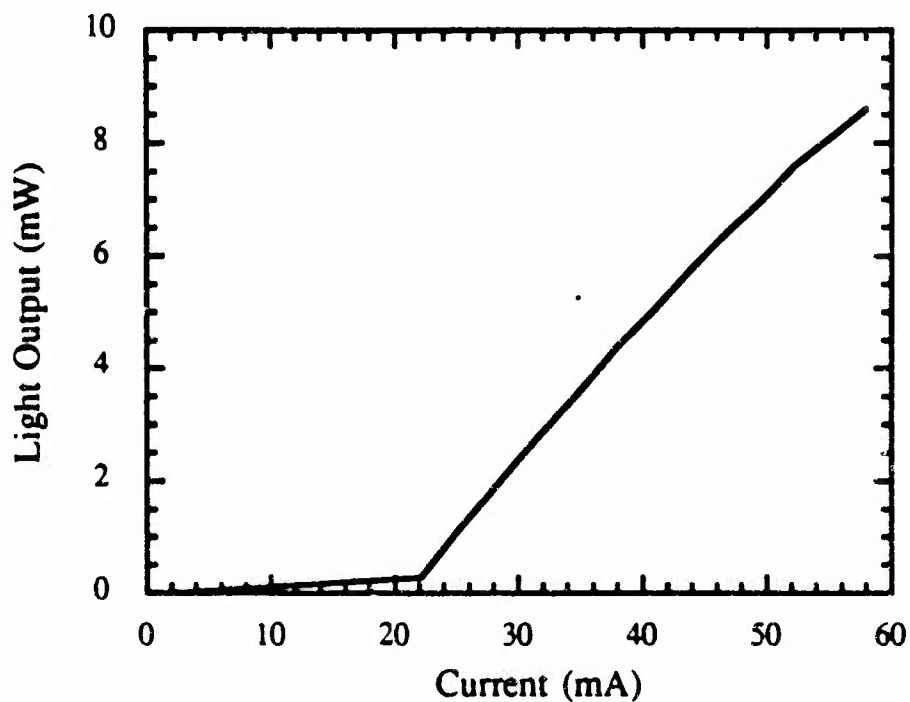


Fig. 12 CW L-I of  $2 \times 400 \mu m$  ridge laser using three  $100 \text{ \AA}$  strained (Al,Ga,In)As quantum wells with homogenous alloy waveguide measured at room temperature.

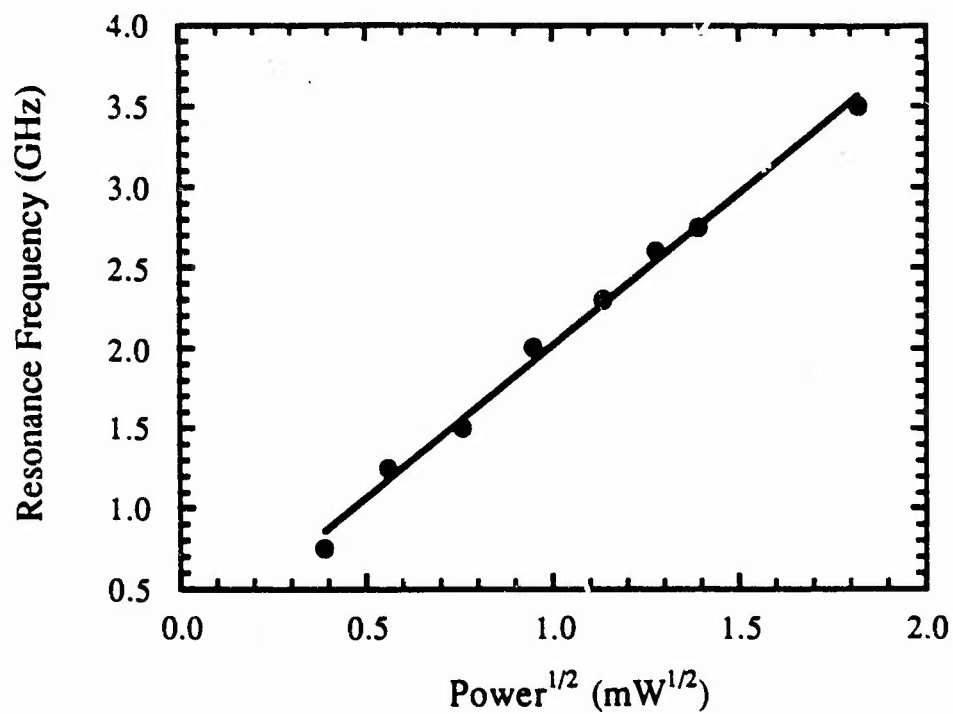


Fig. 13 Resonance frequency determined from RIN measurements as a function of the square root of output power using the device in Fig. 12.

## **SECTION 4**

**Gas-Source Molecular Beam Epitaxy (GSMBE) Growth of InGaAsP**

## 4.1 Introduction

During the this three-year program, we have developed the GSMBE techniques for growth of high quality  $\text{In}_x\text{Ga}_{1-x}\text{As}_y\text{P}_{1-y}$  and delivered to UCSB 44 custom-designed InGaAsP/InP heterostructures for fabrication into lasers and other optoelectronic devices. We have obtained high reflectivity distributed Bragg reflectors using alternating epitaxial layers of InGaAsP and InP at the wavelengths of 1.31 and 1.55  $\mu\text{m}$ . GSMBE InGaAsP material has been used for fabrication of both edge emitting and vertical cavity surface emitting lasers. In addition, we have obtained record-setting performance in high speed InGaAs/InP pin photodetectors.

Heteroepitaxial structures of the quaternary alloy  $\text{In}_x\text{Ga}_{1-x}\text{As}_y\text{P}_{1-y}$  lattice matched to InP are widely used in optoelectronic devices operating in the 1.0 to 1.6  $\mu\text{m}$  wavelength range. Precise control of alloy composition is needed for optimum device performance; in particular the growth of epitaxial mirrors using distributed Bragg reflectors (DBR) requires accurate control of both alloy composition and layer thickness to obtain high reflectivity at the desired operating wavelength. A DBR consists of alternating layers of InGaAsP and InP, each layer a quarter wavelength in thickness, with a sufficient number of layers to obtain high reflectivity at wavelengths where the InGaAsP is transparent. DBR are key components in surface emitting lasers and reflection-mode optical modulators, and InGaAsP/InP DBR have been recently reported with a reflectivity of 98% at a wavelength of 1.49  $\mu\text{m}$  [1] and approximately 100% at 1.54  $\mu\text{m}$  [2]. As the wavelength is reduced, the InGaAsP composition must be moved closer to that of InP, the difference in the index of refraction between InGaAsP and InP decreases, and it becomes increasingly difficult to obtain a high reflectivity mirror. In this report, we describe in detail the results of a study of the control of InGaAsP alloy composition during gas-source MBE growth and demonstrate high reflectivity InGaAsP/InP mirrors at wavelengths of 1.3 and 1.55  $\mu\text{m}$ .

## Epitaxial Growth

Nominally lattice-matched films were grown on (100) oriented InP substrates which were degreased and then etched in a solution of  $\text{H}_2\text{SO}_4:\text{H}_2\text{O}_2:\text{H}_2\text{O}$  before loading in the MBE system. The growth temperature was approximately 500°C. The In and Ga molecular beams were provided by conventional effusion cells and  $\text{As}_2$  and  $\text{P}_2$  molecular beams were produced by thermal decomposition of 100%  $\text{AsH}_3$  and 100%  $\text{PH}_3$ , respectively, at 900°C in a single low-pressure gas cracking oven of all Ta construction.

As shown in Fig. 1(a), the feedstock gases  $\text{PH}_3$  and  $\text{AsH}_3$  were mixed before entering the

MBE system in a gas manifold, a technique which is based on the work of Panish and Sumski [3]. The flow rate  $F$  of each gas was controlled by adjusting the pressure  $P$  against the conductances  $G$  and  $kG$  of the tubing in gas mixing manifold. No mass flow controllers were used. Under normal operating conditions, the total flow rate  $F_1 + F_2$  is approximately a linear function of the total inlet pressure  $P_1 + P_2$ , as long as the pressure at node  $N$  is larger than the smaller of  $P_1$  or  $P_2$ . On the other hand, the flow ratio  $F_1/F_2$ , which controls the group-V composition of the epitaxial film, is a nonlinear function of the pressure ratio  $P_2/P_1$ . For our gas manifold, the conductance ratio  $k$  is about 2.0 and the calculated dependence of  $F_1/F_2$  on  $P_1/P_2$  is shown in Figure 1(b) along with the operating points for three different InGaAsP compositions. With this system, we can easily control flow ratios as high as 15:1 with better than  $\pm 0.4\%$  reproducibility at a total flow rate of 10 sccm.

InGaAsP films of 1-2  $\mu\text{m}$  thickness with compositions corresponding to bandgap emission at wavelengths from 1.1 to 1.6  $\mu\text{m}$  were grown over a range of V/III flux ratios. Room temperature photoluminescence (PL) and double crystal x-ray (DCXR) diffraction were used to determine the bandgap, lattice mismatch, and alloy composition [4]. The results are summarized in Figure 2, where the filled circles represent the measured bandgap wavelength as a function of the fraction of  $\text{PH}_3$  in the total gas flow and the solid curve is the bandgap wavelength as a function of phosphorous content in the film [4]. At each data point the In mole fraction  $x$  was chosen to provide a lattice mismatch of  $\leq 2 \times 10^{-3}$ . Also shown in Fig. 2 are the GSMBE data of Lambert et al. [5] along with data for growth at 555°C by chemical beam epitaxy (CBE) [6] and at 620°C by low pressure metalorganic chemical vapor deposition (MOCVD) [7], all of which also used  $\text{AsH}_3$  and  $\text{PH}_3$  for the group-V source gases. Most of the experimental points lie above the solid curve indicating that As is more readily incorporated than P during InGaAsP growth, regardless of the growth technique. For films in the equivalent composition range of 1.0-1.4  $\mu\text{m}$ , our GSMBE data and that of Lambert et al. [5] appears to indicate a somewhat larger ratio of the As-to-P sticking coefficients than for CBE but a considerably smaller ratio than for MOCVD. For our GSMBE growths, the maximum value of the  $\text{As}_2/\text{P}_2$  sticking coefficient ratio was found to be approximately 6:1. Thus the  $\text{AsH}_3:\text{PH}_3$  flow ratio was easily controlled over the entire InGaAsP composition range by using the pressure control system of Fig. 1. This was demonstrated by reproducibly obtaining a lattice mismatch of less than  $5 \times 10^{-4}$  with a deviation of less than 10 nm at the intended bandgap wavelength of 1.15  $\mu\text{m}$ . Furthermore, the InGaAsP layers were of high quality as evidenced by (400) DCXR linewidths as small as 21 arcsec for a 2  $\mu\text{m}$  thick film and satellite peak widths as small as 13 arcsec in a 20 period InGaAsP(1.15 $\mu\text{m}$ )/InP superlattice. Room temperature PL spectra exhibited intense peaks with full width at half maximum (FWHM) widths typically 50 to 80 meV (see Fig. 4). At an equivalent composition of 1.39  $\mu\text{m}$ , low

temperature PL spectra exhibited band-to-band emission with a FWHM of 4.6 meV, similar to InGaAsP grown by CBE [6]. Unintentionally doped InGaAsP films were n-type with electron concentrations of  $(1-3) \times 10^{16} \text{ cm}^{-3}$ .

The incorporation of As and P was found to be a function of the V/III ratio during GSMBE growth. Figure 4 shows the measured As mole fraction  $y$  as a function of the estimated V/III flux ratio for three different InGaAsP samples. The data in Fig. 3 was obtained by keeping the substrate temperature, In/Ga flux ratio, and  $\text{As}_2/\text{P}_2$  flux ratio constant and increasing the total gas flow in steps during the GSMBE growth. No measurable effect was found on the In mole fraction  $x$ . As seen in Fig. 3,  $y$  increases with the V/III flux ratio and the effect of the V/III flux ratio on  $y$  decreases as the nominal As content increases, with no discernable effect at  $y \approx 0.8$  (i.e., equivalent composition of  $1.55 \mu\text{m}$ ). From Fig. 2 it is apparent that  $\text{As}_2$  is preferentially incorporated in films with  $y$  less than about 0.6. Although increasing the V/III flux ratio increases the  $\text{As}_2$  and  $\text{P}_2$  beam fluxes in the same proportion, the film composition should become increasingly As-rich as the V/III flux ratio is increased, in agreement with data of Fig. 3. During growth of films with higher As content (i.e.,  $y = 0.8$  in Fig. 3),  $\text{As}_2$  and  $\text{P}_2$  are incorporated with equal ease and no dependence of  $y$  on V/III flux ratio is found. Similar results for GSMBE InGaAsP have been reported by Lambert, et al. [5] and the preferential incorporation of  $\text{As}_2$  was first reported by Arthur and Lepore who studied the MBE growth of GaAsP using  $\text{As}_2$  and  $\text{P}_2$  [8].

### 4.3 Results And Discussion

Two types of mirrors have been grown and characterized. The first was designed to operate at  $1.3 \mu\text{m}$  and used a quaternary of  $1.15 \mu\text{m}$  composition. The second operated at  $1.55 \mu\text{m}$  and used InGaAsP of  $1.42 \mu\text{m}$  composition.

The first type of InGaAsP/InP DBRs were grown on  $(100)\text{n}^+$  InP substrates to provide high reflectivity in the wavelength range of  $1.1$  to  $1.4 \mu\text{m}$ . Each heterostructure was doped with Si at a carrier concentration of  $(8-10) \times 10^{17} \text{ cm}^{-3}$  and included a  $100 \text{ nm}$  InP buffer layer and a  $500 \text{ nm}$  InP protective cap layer. Transmission electron microscopy (TEM) was performed at the Solar Energy Research Institute by K. Jones and M. Al-Jassim. Using a Philips CM-30 microscope operating at  $300 \text{ kV}$ , a typical  $[011]$  dark field image of a DBR is shown in Fig. 5. In this sample with 35.5 periods, the InGaAsP layers (dark contrast) and InP layers (light contrast) are seen to be uniform in thickness with the same period of  $171.5 \pm 5.1 \text{ nm}$  over the entire  $6.08 \mu\text{m}$  of the DBR. Furthermore, high resolution lattice images (not shown) indicated an abruptness of 1-2 monolayers at the InP-to-InGaAsP interface and 2-3 monolayers at the InGaAsP-to-InP interface.



Just prior to growth of each DBR, we grew a calibration sample to check the InGaAsP bandgap, lattice mismatch, and growth rate. The calibration sample consisted of a relatively short period superlattice (SL) covered by a thick layer of the InGaAsP material. The period of the SL was chosen to give the maximum sensitivity to thickness measurement by DCXR (i.e.,  $\pm 0.3$  nm). Figure 6 shows the DCXR spectrum for such a typical calibration sample. The growth rate is obtained from the SL period, the lattice mismatch from the positions of the InP substrate and InGaAsP  $r$  peaks, and the bandgap from RT PL of the top layer. Final corrections were then made to the growth timing, effusion cell temperatures, or gas flow rates before growth of the mirror heterostructure.

Figure 7 shows the reflectivity spectrum of a 35.5 period InP/InGaAsP ( $1.15\ \mu\text{m}$ ) mirror after removal of the InP cap layer. The reflectivity was measured at approximately  $15^\circ$  away from normal incidence using a calibrated double beam, double grating spectrophotometer. A freshly evaporated gold mirror was used as the reference, and the reflectivity of the gold was included in calculating the magnitude of the reflectivity. For verification of the peak reflectivity, it was also measured using a  $1.320\ \mu\text{m}$  wavelength laser. The spectrum was modeled by the transmission matrix method [9] including refractive index dispersion [10] and assuming no loss. The layer thicknesses of  $97.4\ \text{nm}$  for InGaAsP and  $103.0\ \text{nm}$  for InP were obtained by fitting the reflectivity data and agreed within 1% with the results of DCXR diffraction and TEM measurements. The maximum measured reflectivity was  $96 \pm 2\%$  at a wavelength of  $1.31\ \mu\text{m}$ , while the model predicts a peak reflectivity of 97.8% for 35.5 periods. The lateral uniformity was excellent with a variation in the peak wavelength of less than  $10\ \text{nm}$  over a region of 1.5 inches in extent on a 2-inch diameter wafer. To the best of our knowledge, the above result is the shortest wavelength yet reported for a InGaAsP/InP epitaxial mirror. We have also used  $1.15\ \mu\text{m}$  InGaAsP to fabricate a mirror which exhibited a reflectivity of 97% at a wavelength of  $1.24\ \mu\text{m}$ .

The second type of DBRs was designed to operate at a wavelength of  $1.55\ \mu\text{m}$  and used alternating layers of InGaAsP ( $1.42\ \mu\text{m}$ ) and InP. The measured reflectivity spectrum of a  $1.55\ \mu\text{m}$  mirror and the  $1.31\ \mu\text{m}$  mirror of Figure 7 are shown in the normalized plot of Figure 8. The maximum reflectivity of the  $1.55\ \mu\text{m}$  mirror was estimated to be 97-99% for 39.5 periods, very similar to the best previously reported for any mirror operating at  $1.55\ \mu\text{m}$  [2]. Also note that the optical bandwidth is much wider at  $1.55\ \mu\text{m}$  compared to that at  $1.31\ \mu\text{m}$ , since the difference in refractive index between the InGaAsP and the InP is larger in the  $1.55\ \mu\text{m}$  mirror.

In conclusion, we have demonstrated high quality InGaAsP can be reproducibly grown

by GSMBE using pressure control of the feedstock gases  $\text{AsH}_3$  and  $\text{PH}_3$ . Using alternating layers of InGaAsP and InP we have achieved 96% reflectivity in a DBR operating at a wavelength of 1.31  $\mu\text{m}$ , 97% at 1.24  $\mu\text{m}$ , and approximately 99% at 1.55  $\mu\text{m}$ .

## References

1. Y. Imajo, A. Kasukawa, S. Kashiwa, and H. Okamoto, Japan J. Appl. Phys. 29, L1130 (1990).
2. F. S. Choa, K. Tai, W. T. Tsang, and S. N. G. Chu, "High Reflectivity 1.55 Micron InP/InGaAsP Surface-Emitting-Laser Mirror Grown by Chemical Beam Epitaxy," Paper MB.6, Topical Meeting on Epitaxial Materials for Optoelectronic Devices, Newport Beach, CA, (1991).
3. M. B. Panish and S. Sumski, J. Appl. Phys. 55, 3571 (1984).
4. R. L. Moon, G. A. Antypas, and L. W. James, J. Electron. Mater. 3, 635 (1974).
5. M. Lambert, L. Goldstein, A. Perales, F. Gaborit, C. Starck, and J-L. Lieven, J. Crystal Growth 111, 495 (1991).
6. W. T. Tsang, E. F. Schubert, T. H. Chiu, J. E. Cunningham, E. G. Burkhart, J. A. Ditzenberger, and E. Agyekum, Appl. Phys. Lett. 51, 761 (1987).
7. P. Wiedemann, M. Klenck, W. Korber, U. Koerner, R. Weinmann, E. Zielinski, and P. Speier, J. Crystal Growth 107, 561 (1991).
8. J. R. Arthur and J. J. Lepore, J. Vac. Sci. Technol. 6, 545 (1969).
9. See for example E. Hecht and A. Zajac, Optics, Addison-Wesley Publishing Co. (Boston), 1974.
10. C. H. Henry, L. F. Johnson, R. A. Logan, and D. P. Clarke, IEEE J. Quant. Electron QE-21, 1887 (1985).

## Journal Publications

1. D. L. Crawford, Y. G. Wey, A. Mar, J. E. Bowers, M. J. Hafich, and G. Y. Robinson, "High Speed InGaAs/InP p-i-n Photodiodes Fabricated on a Semi-Insulating Substrate", *IEEE Photonics Technol. Lett.* 2 (9), 647 (September 1990).
2. M. J. Hafich, H. Y. Lee, P. Silvestre, and G. Y. Robinson, "GSMBE Growth of GaAs at Low AsH<sub>3</sub> Cracking Temperatures", *J. Crystal Growth* 111, 507 (1991).
3. Y. G. Wey, D. L. Crawford, K. Giboney, J. E. Bowers, M. J. Rodwell, P. Silvestre, M. J. Hafich, and G. Y. Robinson, "Ultrafast Graded Double Heterostructure GaInAs/InP p-i-n Photodiode", *Appl. Phys. Lett.* 58 (19), 2156 (13 May 1991).
4. P. Silvestre, M. J. Hafich, T. Vogt, A. Nanda, G. Y. Robinson, J. J. Dudley, J. E. Bowers, K. M. Jones, and M. M. Al-Jassim, "Gas Source MBE Growth of InGaAsP for 1.3 micron Distributed Bragg Reflectors", *J. Vac. Sc. Technol. B* 10 (2), 956 (Mar/Apr 1992).
5. J. G. Wasserbauer, J. E. Bowers, M. J. Hafich, P. Silvestre, L. M. Woods, and G. Y. Robinson, "Specific Contact Resistivity in InGaAs/InP p-Isotype Heterojunctions", submitted to *Electronic Letts.*, July 1992.

## Conference Presentations

1. Y. G. Wey, D. L. Crawford, J. E. Bowers, F. Storz, M. J. Hafich, and G. Y. Robinson, "Design of High Speed GaInAs/InP p-i-n Photodectors", Second International Conference on Indium Phosphide and Related Materials, Denver, April 1990.
2. M. J. Hafich, H. Y. Lee, P. Silvestre, and G. Y. Robinson, "GSMBE Growth of GaAs at Low AsH<sub>3</sub> Cracking Temperatures", Sixth International Conference on Molecular Beam Epitaxy, San Diego, August 1990.
3. D. L. Crawford, Y. G. Wey, J. E. Bowers, M. J. Hafich, and G. Y. Robinson, "GaInAs p-i-n Photodetectors on Semi-insulating Substrates", SPIE Conference, San Jose, September 1990.
4. Y. G. Wey, D. L. Crawford, J. E. Bowers, M. J. Hafich, and G. Y. Robinson, "High Speed InGaAs/InP p-i-n Photodiode on Semi-Insulating Substrate", First DARPA/RADC Conference on Photonics, Monterey, December, 1990.

5. Y. G. Wey, K. Giboney, D. L. Crawford, J. E. Bowers, M. Rodwell, P. Silvestre, M. J. Hafich, and G. Y. Robinson, "Ultrafast Graded Double Heterostructure p-i-n Photodiode", IEEE/OSA Picosecond Electronics and Optoelectronics Topical Meeting, Salt Lake City, March 1991.
6. D. L. Crawford, Y. G. Wey, K. Giboney, M. J. Rodwell, J. E. Bowers, P. Silvestre, M. J. Hafich, and G. Y. Robinson "3.8 ps FWHM Impulse Response of a Graded Double Heterojunction P-I-N Photodiode Fabricated on a Semi-Insulating Substrate", International Conference on InP and Related Materials, Cardiff, Wales, UK, April 1991.
7. P. Silvestre, M. J. Hafich, T. Vogt, A. Nanda, G. Y. Robinson, J. J. Dudley, J. E. Bowers, K. M. Jones, and M. M. Al-Jassim, "Gas Source MBE Growth of InGaAsP for 1.3 micron Distributed Bragg Reflectors", Eleventh Molecular Beam Workshop, Austin, September 1991.
8. J. J. Dudley, D. L. Crawford, J. E. Bowers, P. Silvestre, and G. Y. Robinson, "Temperature Dependence and Material Properties of InGaAsP/InP Mirrors," Fourth International Conference on Indium Phosphide and Related Materials, Newport, April 1992.
9. J. G. Wasserbauer, J. E. Bowers, H. J. Hafich, P. Silvestre, L. M. Woods, and G. Y. Robinson, "Specific Contact Resistivity of InGaAs/InP p-Isotype Heterojunctions", Fourth International Conference on Indium Phosphide and Related Materials, Newport, April 1992.
10. G. Y. Robinson, "Gas-Source Molecular Beam Epitaxy of III-V Semiconductors" (invited paper), Sixth Canadian Semiconductor Conference, Ottawa, August 1992.

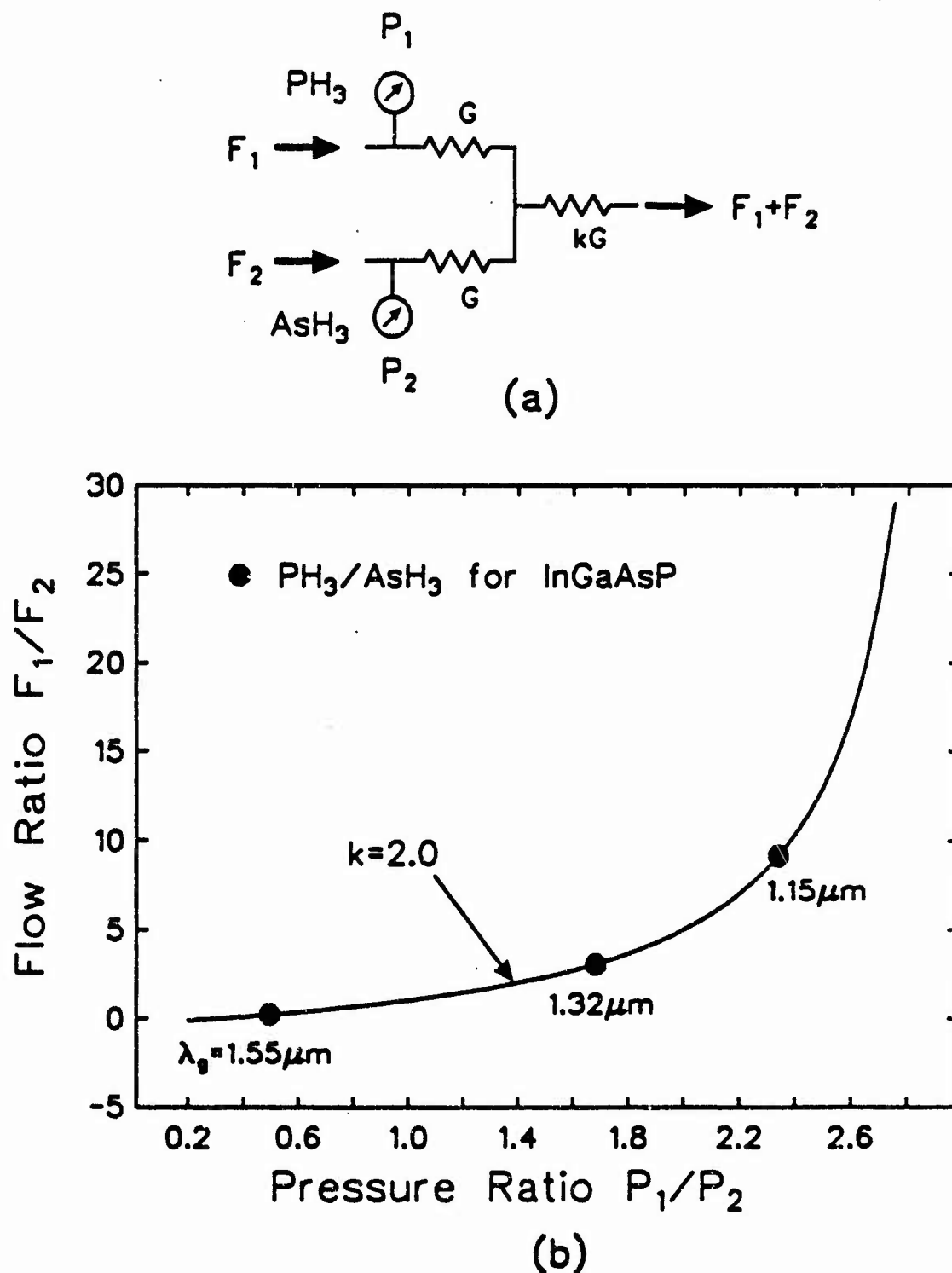


Fig. 1 Pressure control of hydride gas flow for GSMBE. (a) Schematic diagram of gas manifold. (b) Flow ratio as a function of pressure ratio for gas manifold with conductance ratio  $k = 2.0$ . The operating points for three different InGaAsP composition are shown for  $\text{PH}_3$  as gas 1 and  $\text{AsH}_3$  as gas 2.

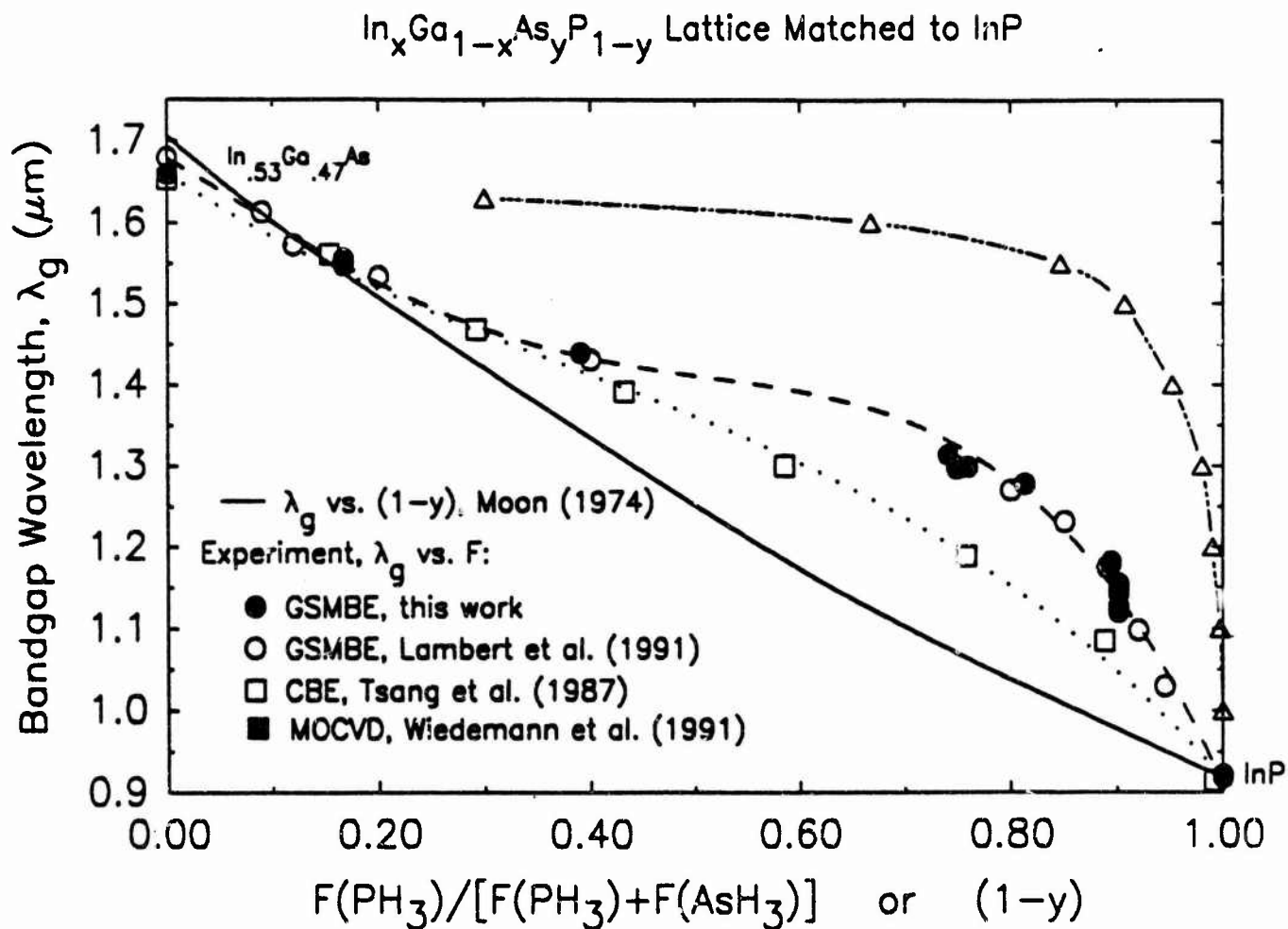


Fig. 2 The bandgap wavelength as a function of fraction of  $\text{PH}_3$  in the gas flow and as a function of the phosphorous mole fraction  $(1-y)$  in  $\text{InGaAsP}$  lattice matched to  $\text{InP}$ . The solid curve is from Moon et al. [4] while the open circles are from Lambert et al. [5], the squares from Tsang et al. [6], and the triangles from Wiedemann et al. [7].

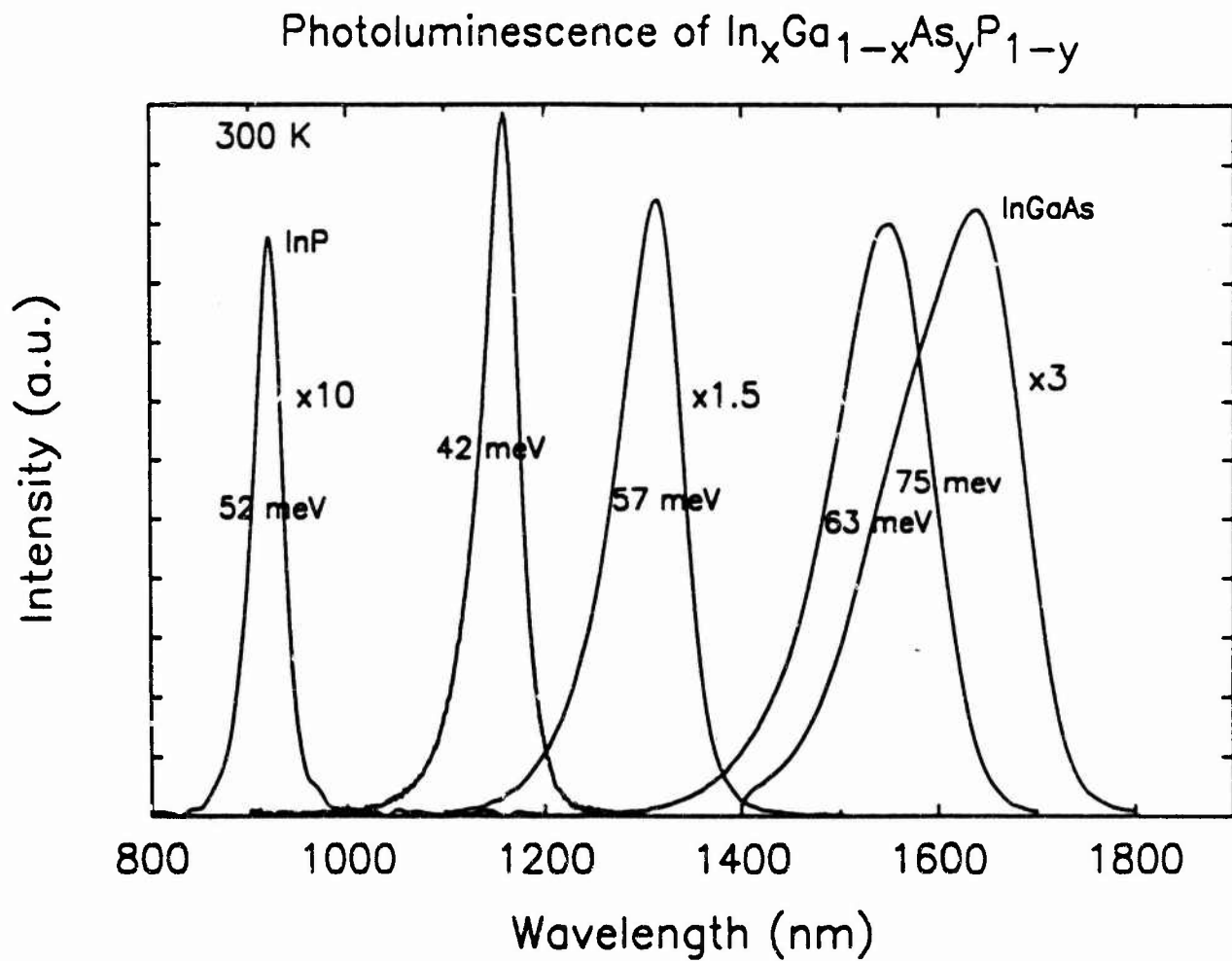


Fig. 3 Room-temperature photoluminescence spectra of InGaAsP films grown by GSMBE.



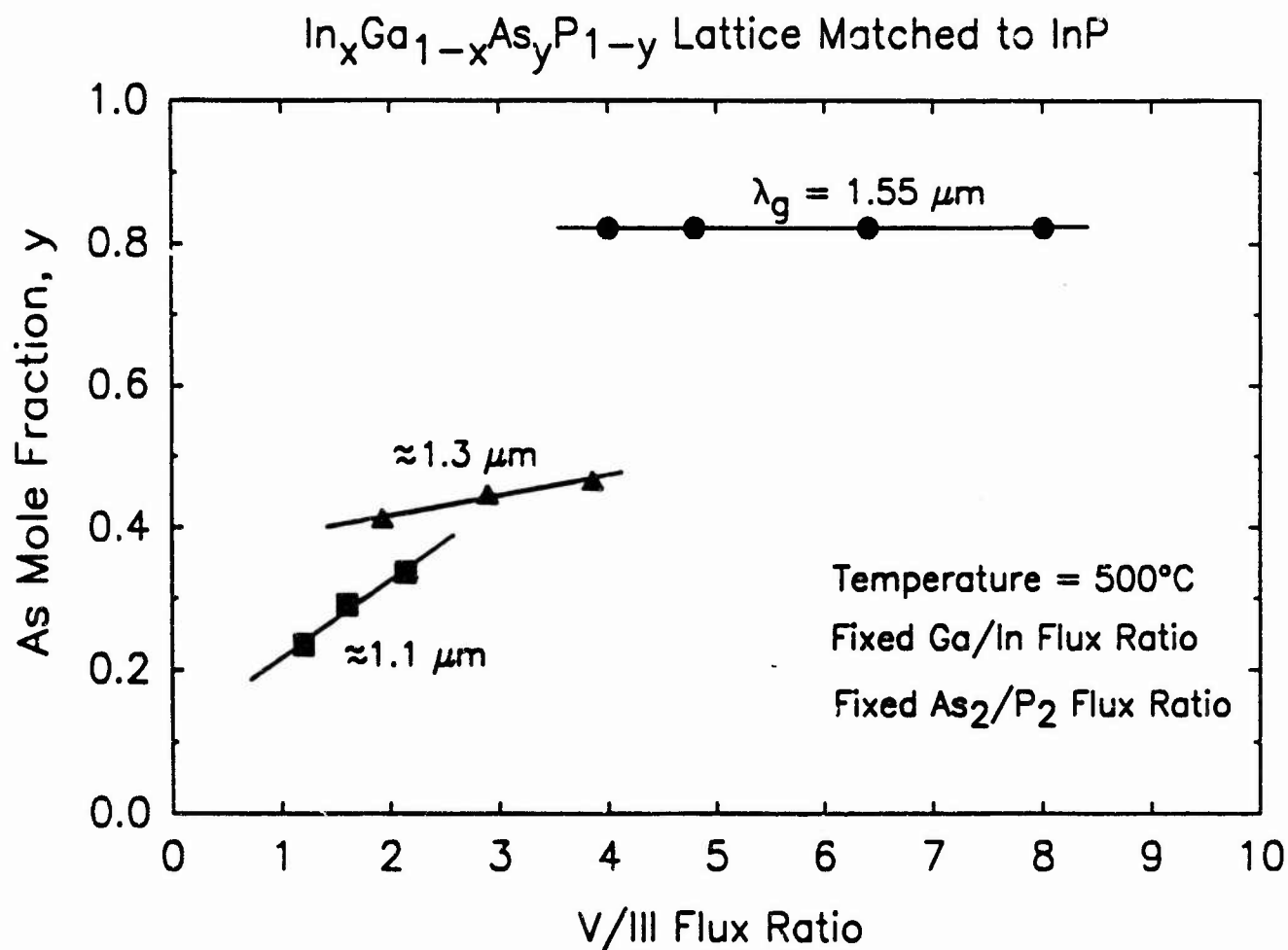


Fig. 4 Arsenic mole fraction as a function of V/III molecular flux ratio for InGaAsP with equivalent compositions 1.1, 1.3, and 1.55  $\mu\text{m}$ .

# InGaAsP(1.15 $\mu$ m)/InP DBR

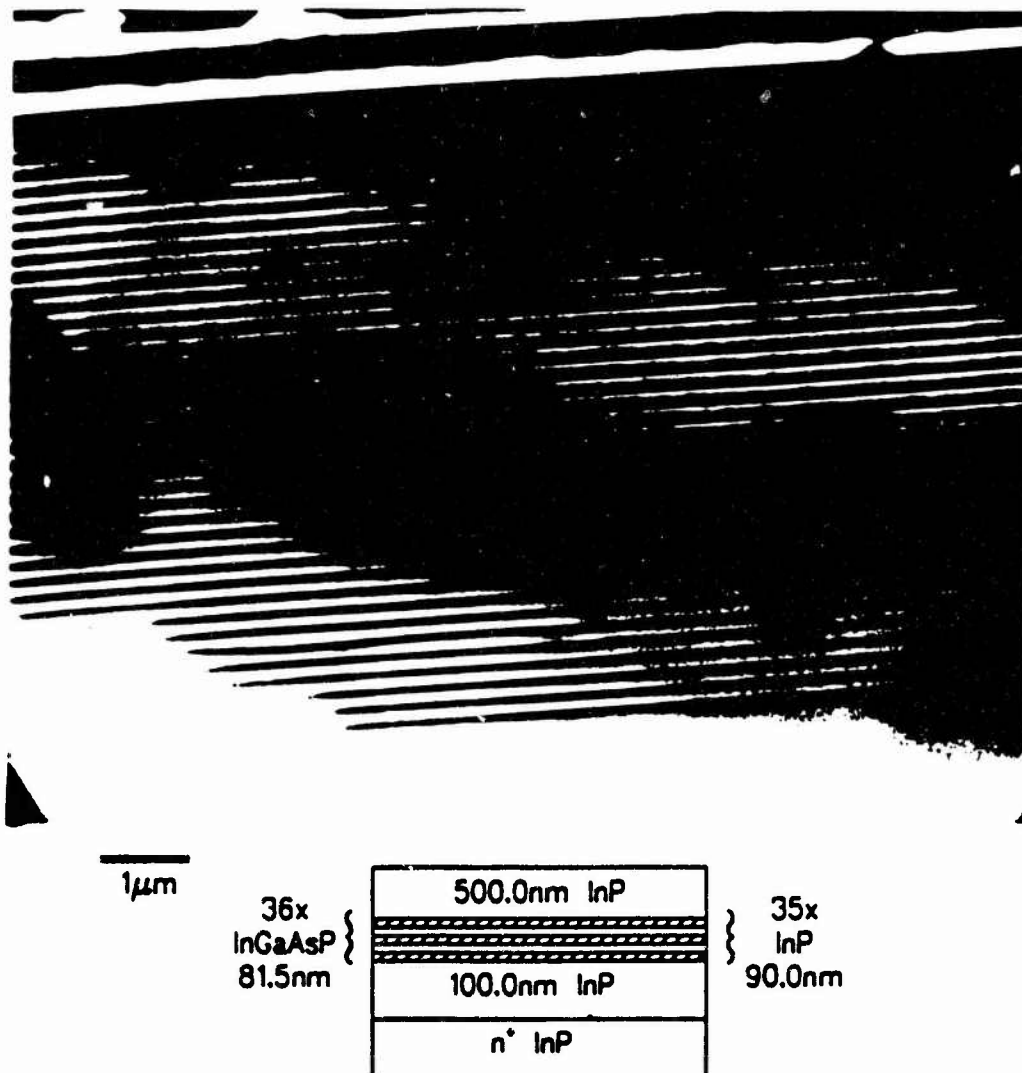


Fig. 5 Dark field [011] TEM cross-section of an InGaAsP(1.15  $\mu$ m)/InP distributed Bragg reflector grown by GSMBE. The insert shows the thicknesses obtained by TEM.

# InGaAsP(1.15 $\mu$ m)/InP 20 Period Superlattice

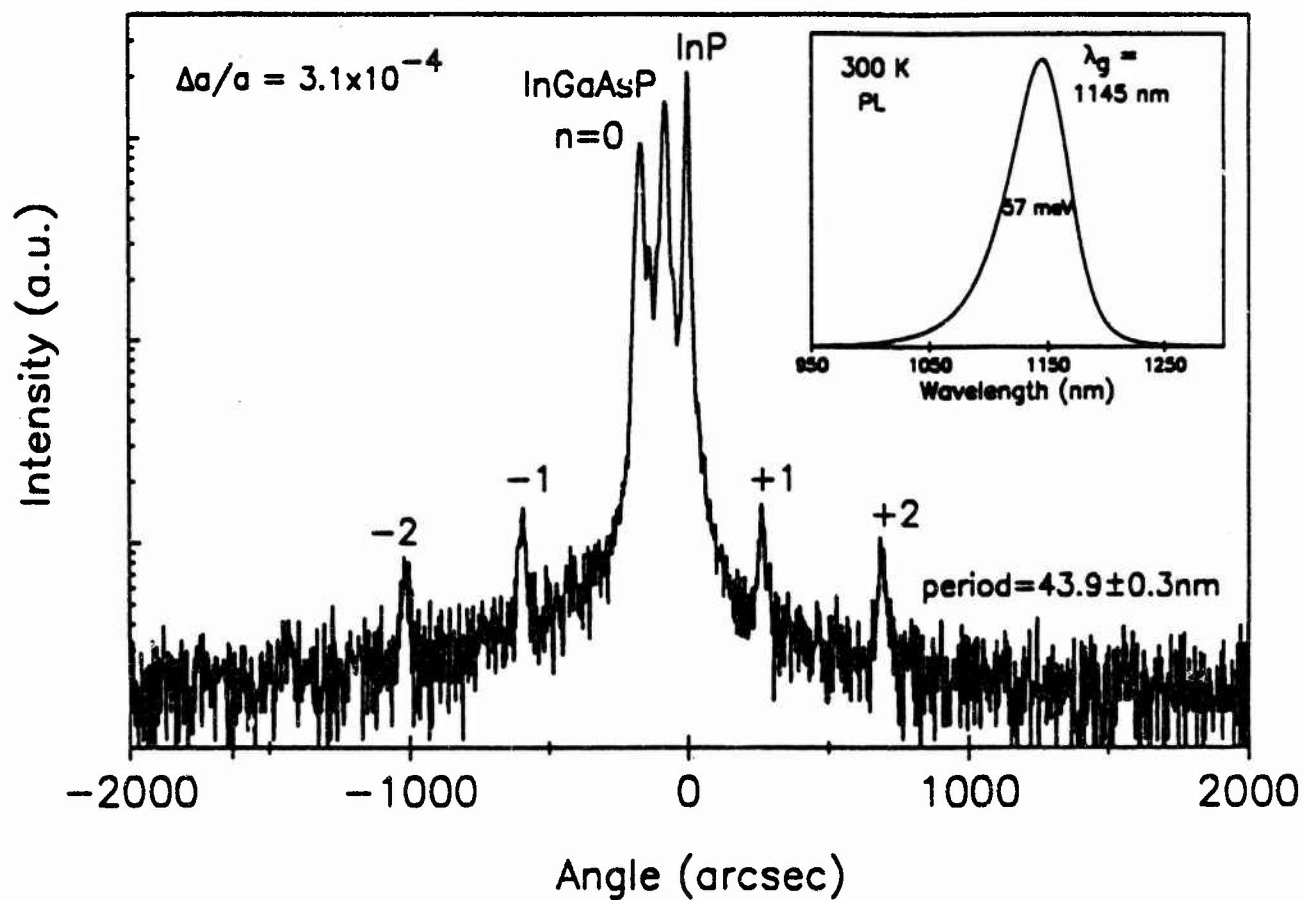


Fig. 6 Double crystal x-ray diffraction spectrum of an InGaAsP/InP superlattice calibration sample. The insert shows the 300K PL spectrum.

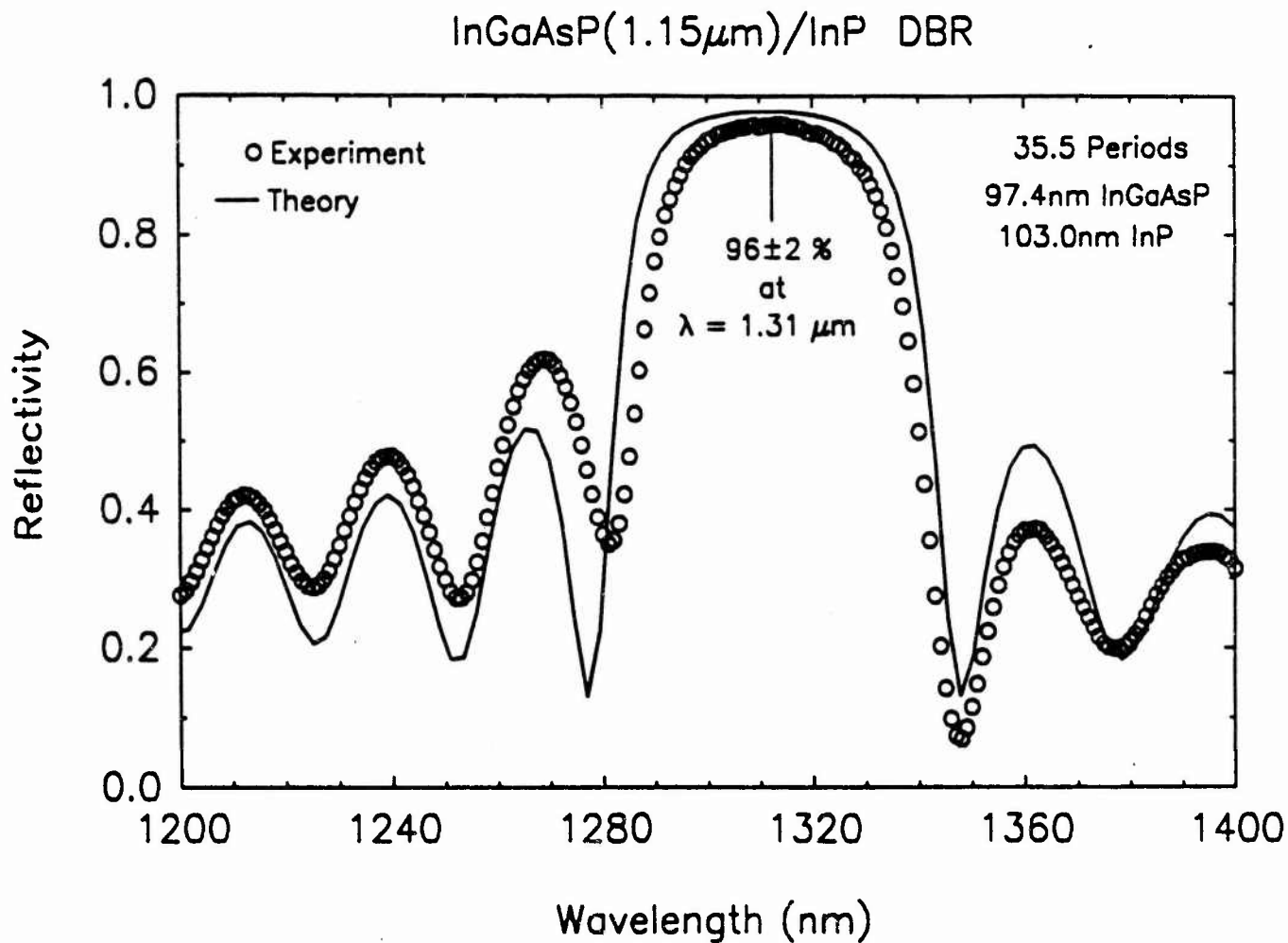


Fig. 7 The optical reflectivity spectrum for a distributed Bragg reflector consisting of 35.5 periods of 97.4 nm of InGaAsP(1.15  $\mu\text{m}$ ) and 103.0 nm of InP.

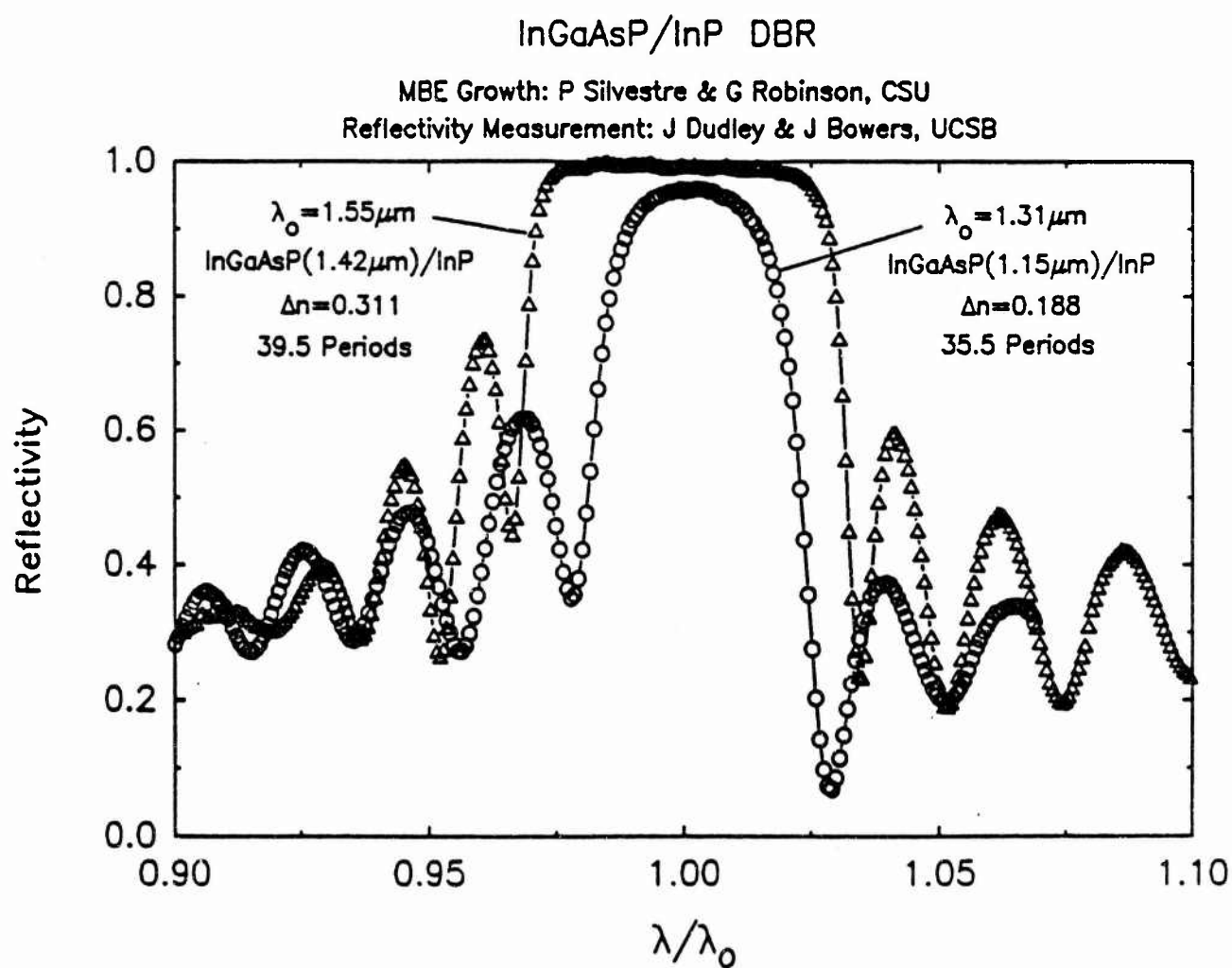


Fig. 8 The measured reflectivity spectrum of two DBRs, one centered at 1.55  $\mu\text{m}$  and the other at 1.31  $\mu\text{m}$  (same spectrum as in Fig. 7).

# DISTRIBUTION LIST

addresses	number of copies
ATTN:JOSEPH LORENZO RL/EROC 80 SCOTT RD BLDG 1128 HANSCOM AFB, MA 01731-2090	5
J. BOWERS UNIVERSITY OF CA /SANTA BARBARA OFFICE OF RESEARCH DEVELOPMENT SANTA BARBARA CA 39106	5
RL/SUL TECHNICAL LIBRARY 26 ELECTRONIC PKY GRIFFISS AFB NY 13441-4514	1
ADMINISTRATOR DEFENSE TECHNICAL INFO CENTER DTIC-FDAC CAMERON STATION BUILDING 5 ALEXANDRIA VA 22304-6145	2
ADVANCED RESEARCH PROJECTS AGENCY 3701 NORTH FAIRFAX DRIVE ARLINGTON VA 22203-1714	1
WRIGHT LABORATORY/MTEL WRIGHT-PATTERSON AFB OH 45433	1
ADVISORY GROUP ON ELECTRON DEVICES ATTN: DOCUMENTS 2011 CRYSTAL DRIVE,SUITE 307 ARLINGTON VA 22202	2

***MISSION  
OF  
ROME LABORATORY***

**Mission.** The mission of Rome Laboratory is to advance the science and technologies of command, control, communications and intelligence and to transition them into systems to meet customer needs. To achieve this, Rome Lab:

- a. Conducts vigorous research, development and test programs in all applicable technologies;
- b. Transitions technology to current and future systems to improve operational capability, readiness, and supportability;
- c. Provides a full range of technical support to Air Force Materiel Command product centers and other Air Force organizations;
- d. Promotes transfer of technology to the private sector;
- e. Maintains leading edge technological expertise in the areas of surveillance, communications, command and control, intelligence, reliability science, electro-magnetic technology, photonics, signal processing, and computational science.

The thrust areas of technical competence include: Surveillance, Communications, Command and Control, Intelligence, Signal Processing, Computer Science and Technology, Electromagnetic Technology, Photonics and Reliability Sciences.